8 Surface Characterization

Mandla A. Tshabalala, Joseph Jakes, Mark R. VanLandingham, Shaoxia Wang, and Jouko Peltonen

CONTENTS

8.1 Overview of Surface Properties 217
8.2 Microscopic Methods for Characterizing Surface Properties 218
8.2.1 Confocal Laser Scanning Microscopy (CLSM) 218
8.2.2 Scanning Electron Microscopy (SEM) 220
8.2.3 Atomic Force Microscopy (AFM) 222
8.2.4 Nanoindentation 225
8.3 Spectroscopic Methods for Characterizing Surface Properties 230
8.3.1 Molecular Spectroscopy 230
8.3.2 Electron Spectroscopy 232
8.3.3 Mass Spectroscopy 236
8.4 Thermodynamic Methods for Characterizing Surface Properties 241
8.4.1 Contact Angle Analysis (CAA) 241
8.4.2 Inverse Gas Chromatography (IGC) 244
8.4.3 Total Surface Energy 245
8.4.3.1 Dispersive Component of the Total Surface Energy 245
8.4.3.2 Acid—Base Component of the Total Surface Energy 245
8.5 Conclusions and Outlook 247
References 247

8.1 OVERVIEW OF SURFACE PROPERTIES

Surface properties of wood play an important role when wood is used or processed into different commodities such as siding, joinery, textiles, paper, sorption media, or wood composites. Thus, for example, the quality and durability of a wood coating are determined by the surface properties of the wood and the coating. The same is true for wood composites where the efficiency of stress transfer from the wood component to the nonwood component is strongly influenced by the surface properties of both components.

Surface properties of wood can be divided into two major groups: physical and chemical properties. Physical properties include morphology, roughness, smoothness, specific surface area, and permeability. Chemical properties include elemental and molecular or functional group composition. Taken together these two major groups of properties determine the thermodynamic characteristics of the wood surface such as surface-free energy and surface acid—base acceptor and donor numbers, and mechanical properties such as hardness, modulus of elasticity, and toughness.

Wood has a cellular structure whose cell walls are composed of three major constituents: cellulose, hemicelluloses, and lignin. In addition to these major constituents the cell wall also contains pectins, extractives, and trace metals. The surface properties of wood are, therefore, determined by the morphology of the cell wall at the surface of a wood element (particle, fiber, flake, or chip), and the distribution of the major and minor constituents in the cell wall. Hence, in order to optimize the quality of interaction of the wood surface with a coating, or with the matrix

in a wood composite, the surface properties of both the wood and the coating or the matrix in a composite must be known.

Methods for characterizing surface properties of wood may be divided into four broad categories: microscopic, spectroscopic, thermodynamic, and nanomechanical. Microscopic methods provide information about surface morphology; spectroscopic methods provide information about surface chemistry; thermodynamic methods provide information about the surface energy; and nanomechanical methods provide information about the mechanical strength of wood cell walls.

8.2 MICROSCOPIC METHODS FOR CHARACTERIZING SURFACE PROPERTIES

Many types of microscopic methods are available for characterizing physical properties of surfaces of various materials, but only a few have been particularly useful and productive in characterizing physical properties of wood surfaces. These are confocal laser scanning microscopy (CLSM), scanning electron microscopy (SEM), and atomic force microscopy (AFM).

8.2.1 CONFOCAL LASER SCANNING MICROSCOPY (CLSM)

A typical CLSM instrument consists of a light microscope equipped with scanning mechanisms and motorized focus, a laser source (He/Ne, krypton, or argon), and computer system with software for instrument control, and for three-dimensional (3-D) reconstruction, image processing, and image analysis.

The basic principle of CLSM is illustrated schematically in Figure 8.1. A collimated, polarized laser beam from an aperture is reflected by a beam splitter (dichroic mirror) into the rear of the objective lens and is focused on the specimen. The reflected or emitted, longer-wavelength fluorescent light returning from the specimen passes back through the same lens. The light beam is focused by the beam splitter into a small pinhole, the confocal aperture, to eliminate all the out-of-focus light that comes from regions of the specimen above or below the plane of focus. A photo multiplier tube (PMT) positioned behind the confocal aperture converts the detected in-focus light beam from each specimen point into an analog output signal that is stored in a computer in digital form. A point-by-point digital image is obtained by scanning the beam over an XY plane. The thickness of such an XY image in the Z direction depends on the diameter of the detector pinhole: the more open

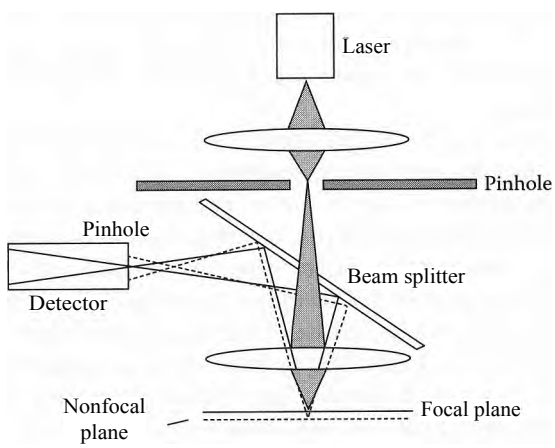

FIGURE 8.1 Principle of CLSM. Out-of-focus light beam from nonfocal plane is excluded from the detector by the confocal detector pinhole. (Courtesy of Lloyd Donaldson, M.Sc. Hons, D. Sc. Cell Wall Biotechnology Center, Forest Research, New Zealand.)

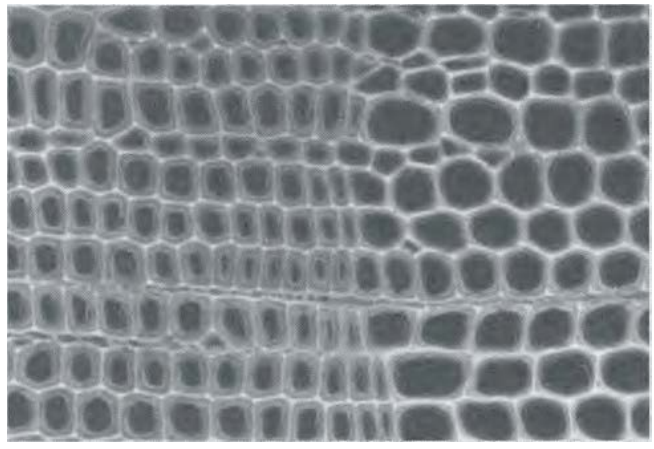

FIGURE 8.2 Transverse view of thick-wall latewood (left) and thin-wall early wood (right) tracheids of *Pinus radiata.* (Micrographs provided by Lloyd Donaldson, M.Sc. Hons, D.Sc. Cell Wall Biotechnology Center, Forest Research, New Zealand.)

the pinhole, the thicker the XY image (Pawley 1990, Boyde 1994, Lichtman 1994, Béland and Mangin 1995, Leica 1999).

Perhaps the greatest advantage of CLSM over other forms of optical microscopy is that it allows 3-D imaging of thick and opaque specimens such as wood surfaces without physically slicing the specimen into sections. Figures 8.2 through 8.4 show 625 μm x 625 p.m micrographs of a wood specimen obtained on a Leica TCS/NT confocal microscope. The wood specimen was stained with acriflavin (Donaldson 2003). The micrographs clearly show the anisotropic morphology of wood surfaces. In transverse view (Figure 8.2) thin-walled early wood and thick-walled late wood tracheids are clearly distinguishable. In the radial view (Figure 8.3) radial bordered pits and an uniseriate heterogeneous ray are clearly visible. In the tangential view (Figure 8.4) uniseriate rays, small tangential pits in late wood, and larger tangential pits in early wood are also clearly visible.

CLSM has also been used in the study of resin distribution in medium density fiberboard (Loxton et al. 2003). In another study, CLSM was used to study the effect of simulated acid rain on coatings for exterior wood panels (Lee et al. 2003).

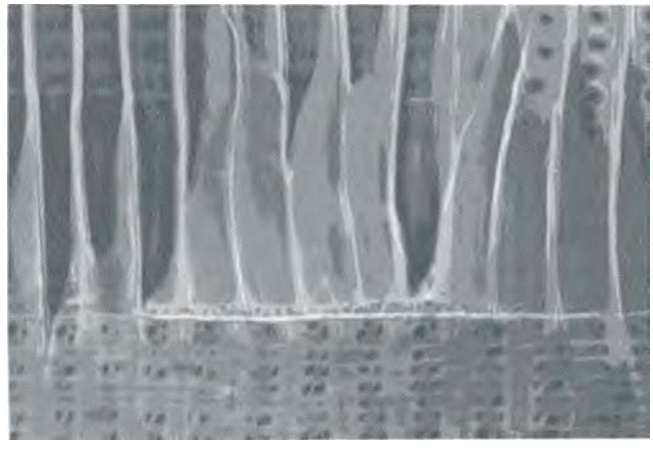

FIGURE **8.3** Radial view of tracheids of *Pinus radiata* showing radial bordered pits (upper left-hand corner) and uniseriate heterogeneous ray (center of micrograph).

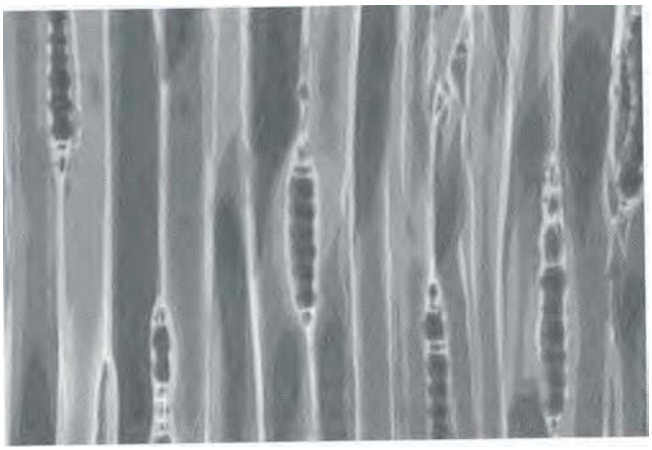

FIGURE 8.4 Tangential view of tracheids of *Pinus radiata* showing fusiform rays, and uniseriate heterogeneous and homogeneous rays.

8.2.2 SCANNING ELECTRON MICROSCOPY (SEM)

The basic principle of SEM is illustrated in Figure 8.5. The primary electron beam, which is produced under high vacuum at the top of the microscope by heating a metallic element, is scanned across the surface of a specimen. When the electrons strike the specimen, a variety of signals are generated, and it is the detection of specific signals that produces an image of the surface, or its elemental composition. The three signals, which provide the greatest amount of information in SEM, are the secondary electrons, backscattered electrons, and x-rays.

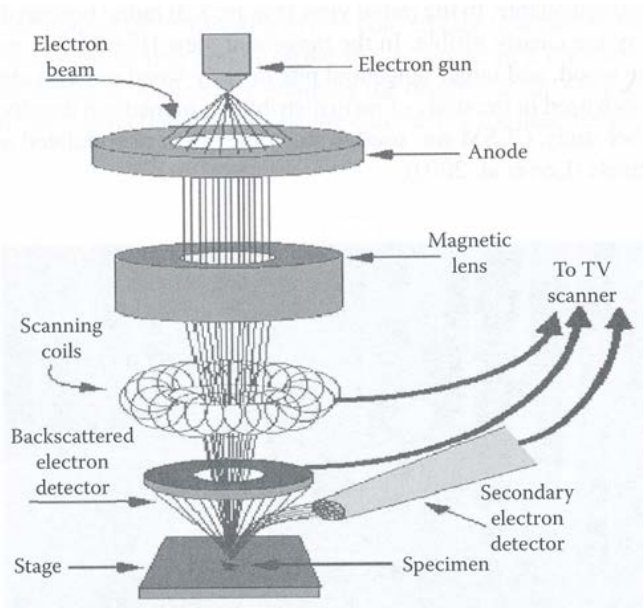

FIGURE 8.5 Principle of SEM. The primary electron beam produced at the top of the microscope by heating of metallic filament is focused and scanned across surface of a specimen by means of electromagnetic coils. Secondary and backscattered electron beams ejected from the surface are collected in detectors, which convert them to a signal that is processed into an image. (Courtesy of Prof. Scott Chumbley, Iowa State University, Materials Science and Engineering Department.)

Secondary electrons are emitted from the atoms occupying the top surface layer, and produce an image of the surface. The contrast in the image is determined by the surface morphology. A high-resolution image can be obtained because of the small diameter of the primary electron beam.

Backscattered electrons are primary beam electrons, which are reflected by the atoms in the surface layers. The contrast in the image produced is determined by the atomic number of the elements in the surface layers. The image will therefore show the distribution of different chemical phases in the specimen surface. Because backscattered electrons are emitted from a depth in the specimen, the resolution in the image is usually not as good as for secondary electrons.

Interaction of the primary beam with atoms in the specimen causes electron shell transitions, which result in the emission of an x-ray. The emitted x-ray has an energy that is characteristic of its parent element. Detection and measurement of x-ray energy permits elemental analysis, and is commonly referred to as energy dispersive x-ray spectroscopy (EDS or EDX or EDXA). EDS can provide rapid qualitative or, with adequate calibration standards, quantitative analysis of elemental composition with a sampling depth of 1-2 μm. X-rays may also be used to form maps or line profiles, showing the elemental distribution in a specimen surface.

One of the latest innovations in SEM is environmental scanning electron microscopy (ESEM). ESEM differs from conventional SEM in two crucial aspects (Danilatos 1993, Donald 2003). First, ESEM allows the introduction of a gaseous environment in the specimen chamber although the electron gun itself is kept under the standard SEM high vacuum. Second, the wood specimens do not need to be coated with a metallic layer, as is the case in conventional SEM.

It should be noted that the gaseous environment in the specimen chamber plays a key role in signal detection (Danilatos 1988, Meredith et al. 1996). As the secondary electrons travel toward the positively charged detector they collide with the gas molecules. Each such collision leads to the generation of an additional daughter electron, so that an amplified cascade of electrons reaches the detector. Along with additional daughter electrons, positive ions are also produced. These positive ions drift down toward the specimen, and hence serve to compensate charge build-up at the surface of nonconductive specimens such as wood. It is for this reason that nonconductive specimens do not need to be coated with a metallic layer to prevent charging artifacts and consequent loss of image quality.

Figures 8.6, 8.7, and 8.8 show ESEM micrographs of specimens prepared from the softwood *Pinus taeda.*

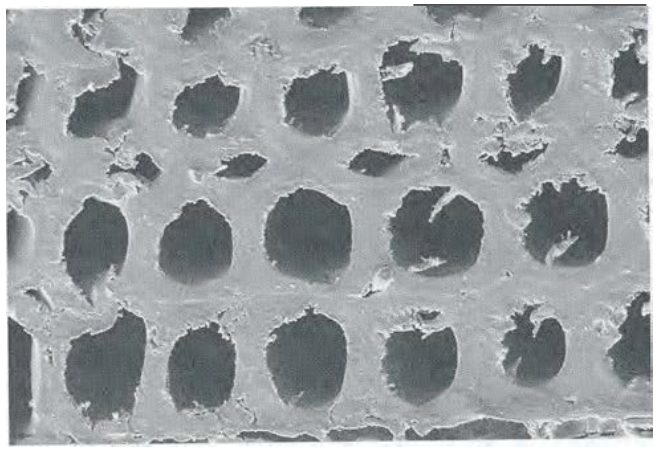

FIGURE 8.6 ESEM micrograph of the softwood *Pinus taeda* showing the transverse surface of thick-walled latewood tracheids. A uniseriate ray is visible above the bottom row of tracheids. (Courtesy T.A. Kuster, USDA Forest Service, Forest Products Laboratory, Madison, WI.)

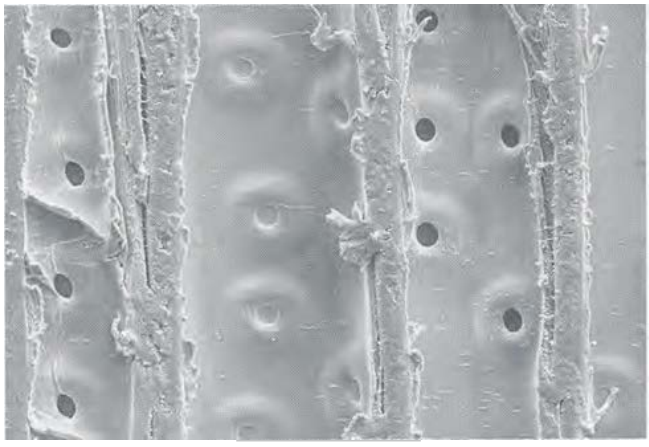

FIGURE 8.7 ESEM micrograph of the softwood *Pinus taeda* showing the radial surface of tracheids. Bordered pits are clearly visible. The warty membrane that lines the lumen is also clearly visible, especially in the left lumen where it has peeled back at some spots. (Courtesy T.A. Kuster, USDA Forest Service, Forest Products Laboratory, Madison, WI.)

8.2.3 ATOMIC FORCE MICROSCOPY (AFM)

The basic principle and application of AFM has been the subject of a number of excellent reviews (Meyer 1992, Frommer 1992, Hoh and Engel 1993, Frisbie et al. 1994, Hanley and Gray 1994, 1995, Louder and Parkinson 1995, McGhie et al. 1995, Rynders et al. 1995, Schaefer et al. 1995, Hansma et al. 1998). In AFM, a probe consisting of a sharp tip (nominal tip radius on the order of 10 nm) located near the end of a microcantilever beam is raster scanned across the surface of a specimen using piezoelectric scanners. Changes in the tip-specimen interaction are often monitored using an optical lever detection system, in which a laser beam is reflected off the cantilever and onto a position-sensitive photodiode. During scanning, a particular operating parameter is maintained at a constant level, and topographic images are generated through a feedback loop between the optical detection system and the piezoelectric scanners.

FIGURE 8.8 ESEM micrograph of the softwood *Pinus taeda* showing the tangential surface of thick-walled latewood tracheids. The tangential surface has relatively fewer bordered pits compared to the radial surface. (Courtesy T.A. Kuster, USDA Forest Service, Forest Products Laboratory, Madison, WI.)

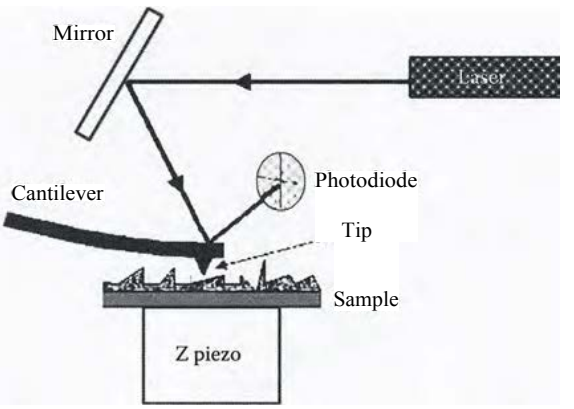

FIGURE 8.9 Schematic diagram of contact mode AFM. The tip makes soft physical contact with the sample. Optical detection of the position of the cantilever leads to a topographic map of the sample surface. (Courtesy of National Physical Laboratory, Teddington, Middlesex, UK, TW11 0LW. © Crown Copyright 2004. Reproduced by permission of the Controller of HMSO.)

Three imaging modes, contact mode, noncontact mode, and intermittent contact or tapping mode can be used to produce a topographic image of the surface. In contact mode (see Figure 8.9), the probe is essentially dragged across the surface of the specimen. During scanning, a constant bend in the cantilever is maintained. A bend in the cantilever corresponds to a displacement of the probe tip, z_t, relative to an undeflected cantilever, and is proportional to the applied normal force, $P = k \bullet z_t$, where k is the cantilever spring constant. As the topography of the surface changes, the z-scanner must move the position of the tip relative to the surface to maintain this constant deflection. Using this feedback mechanism, the topography of the specimen surface is thus mapped during scanning by assuming that the motion of the *z*-scanner directly corresponds to the surface topography. To minimize the amount of applied force used to scan the sample, low-spring constant ($k \leq$ N/m) probes are normally used. However, significant deformation and damage of soft samples (e.g., biological and polymeric materials) often occurs during contact mode imaging in air, because significant force must be applied to overcome the effects of surface roughness or adsorbed moisture as is the case with wood specimens. The combination of a significant normal force, the lateral forces created by the dragging motion of the probe tip across the specimen, and the small contact areas involved result in high contact stresses that can damage either the specimen surface, or the tip, or both. To overcome this limitation, contact mode imaging can be performed under a liquid environment, which essentially eliminates problems due to surface moisture such that much lower contact forces can be used. In fact, the ability to image samples under a liquid environment is often a desirable capability of AFM, but in some cases it might not be practical or feasible. Also, working with liquid cells for many commercial AFM systems can be tricky because of the potential for spills and leaks that can introduce liquid into the scanners.

To mitigate or completely eliminate the damaging forces associated with contact mode, the cantilever can be oscillated near its first bending mode resonance frequency (normally on the order of 100 kHz) as the probe is raster scanned above the specimen surface in either noncontact mode or tapping mode. In noncontact mode (see Figure 8.10), both the tip-specimen separation and the oscillation amplitude are on the order of 1-10 nm, such that the tip oscillates just above the specimen. The resonance frequency and amplitude of the oscillating probe decrease as the specimen surface is approached due to interactions with van der Waals and other long-range forces extending above the surface. These types of forces tend to be quite small relative to the repulsive forces encountered in contact mode. Either a constant amplitude or constant resonance frequency is maintained through a feedback loop with the scanner and, similar to contact mode, the motion of the scanner is used to

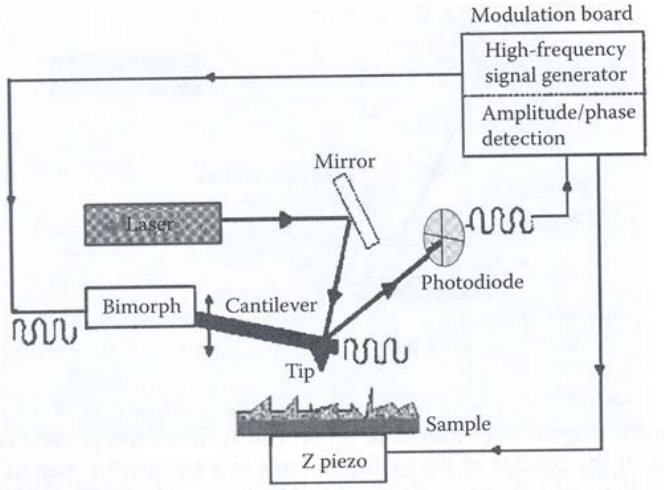

FIGURE 8.10 Schematic diagram of noncontact mode AFM. The cantilever is vibrated near the surface of the sample. Changes in the resonance frequency or vibration amplitude of the cantilever as the tip approaches the surface are used to measure changes in the sample surface topography. (Courtesy of National Physical Laboratory, Teddington, Middlesex, UK, TW11 OLW. © Crown Copyright 2004. Reproduced by permission of the Controller of HMSO.)

generate the topographic image. To reduce the tendency of the tip to be pulled down to the surface by attractive forces, the cantilever spring constant is normally much higher compared to contact mode cantilevers. The combination of weak forces affecting feedback and large spring constants causes the noncontact AFM signal to be small, which can lead to unstable feedback and re quires slower scan speeds than either contact mode or tapping mode. Also, the lateral resolution in noncontact mode is limited by the tip-specimen separation and is normally lower than that in either contact mode or tapping mode.

Tapping mode tends to be more applicable to general imaging in air, particularly for soft samples, as the resolution is similar to contact mode while the forces applied to the specimen are lower and less damaging. In fact, the only real disadvantages of tapping mode relative to contact mode are that the scan speeds are slightly slower and the AFM operation is a bit more complex, but these disadvantages tend to be outweighed by the advantages. In tapping mode, the cantilever oscillates close to its first bending mode resonance frequency, as in noncontact mode. However, the oscillation amplitude of the probe tip is much larger than for noncontact mode, often in the range of 20-200 nm, and the tip makes contact with the sample for a short time in each oscillation cycle. As the tip approaches the specimen, the tip-specimen interactions alter the amplitude, resonance frequency, and phase angle of the oscillating cantilever. During scanning, the amplitude at the operating frequency is maintained at a constant level, called the set-point amplitude, by adjusting the relative position of the tip with respect to the specimen. In general, the amplitude of oscillation during scanning should be large enough such that the probe maintains enough energy for the tip to tap through and back out of the surface layer.

One recent development in tapping mode is the use of the changes in phase angle of the cantilever probe to produce a second image, called a phase image or phase contrast image. This image often provides significantly more contrast than the topographic image and has been shown to be sensitive to material surface properties, such as stiffness, viscoelasticity, and chemical composition. In general, changes in phase angle during scanning are related to energy dissipation during tip-sample interaction and can be due to changes in topography, tip-specimen molecular interactions, deformation at the tip-specimen contact, and even experimental conditions. Depending on the operating conditions, different levels of tapping force might be required to produce an accurate and reproducible

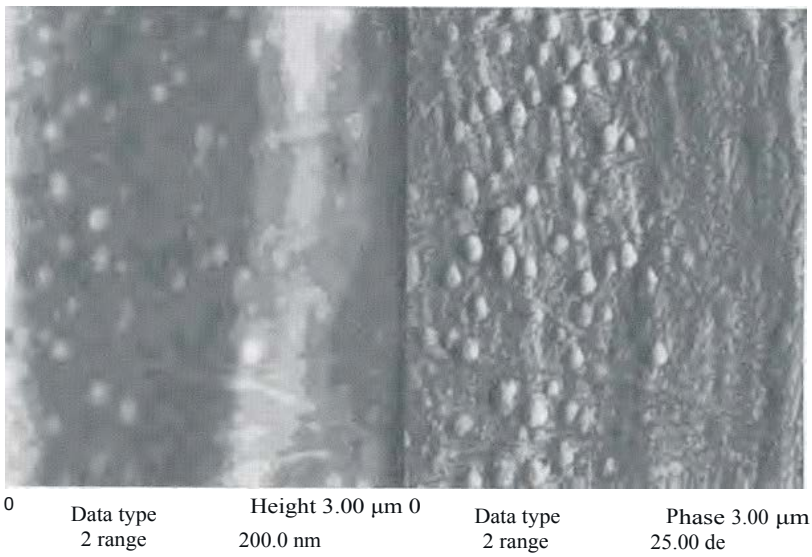

FIGURE **8.11** Topographical (height) and phase contrast images of a bordered pit showing the fibrillar morphology of the margo. The phase contrast image clearly shows the network of nanofibrils that constitute the margo and nodules located close to the pores that permeate the margo.

image of a surface. Also, the amount of tapping force used will often affect the phase image, particularly with regard to whether local tip-specimen interactions are attractive or repulsive.

Similar contrast images can be constructed concurrently with the topographic image in contact mode. One example is lateral force or friction force imaging, in which torsional rotation of the probe is detected while the probe is dragged across the surface in a direction perpendicular to the long axis of the cantilever. Friction force imaging with a chemically modified probe (i.e., a probe that has been coated with a monolayer of a specific organic group) is often referred to as chemical force microscopy. Another example of contrast imaging is force modulation, which combines contact mode imaging with a small oscillation of the probe tip at a frequency far below resonance frequency. This oscillating force should deform softer regions more than harder regions of a heterogeneous sample such that contrast between these regions is observed. In practice, however, the difference between the elastic modulus of the different regions usually has to be substantial (e.g., rubber particles in a plastic, carbon fibers in an epoxy) for contrast to be realized. Thus far, these types of AFM contrast images are purely qualitative due to inaccurate or unknown spring constants, unknown contact geometry, and contributions from different types of surface properties.

Figure 8.11 shows topographic (height) and a phase contrast images of a bordered pit on the surface of the cell wall of a softwood specimen. The images were acquired and recorded simultaneously by tapping mode AFM at ambient conditions, using a Nanoscope MultiMode SPMTM.

8.2.4 NANOINDENTATION

Surface mechanical properties of the wood cell wall can be determined by nanoindentation. Nanoindentation is a type of hardness test in which a specifically shaped probe is pressed into a material and withdrawn following a prescribed loading profile. Load and displacement are continuously monitored and recorded during the experiment. The resulting load-depth trace can be analyzed to assess mechanical properties including, most often, elastic modulus and hardness. The primary advantage of nanoindentation over other types of mechanical tests is its ability to assess mechanical properties from small volumes of materials. Depths of penetration typically range from 10 nm to 10 μm. The initial motivation for development of nanoindentation in the 1980s was to

characterize hard, thin inorganic films Since its inception, however, nanoindentation has proven to be a versatile technique amendable to nearly any material, including ceramics, metals, polymers, and both soft and hard biological tissues. Basic requirements for a nanoindenter include precise instrumentation to separately measure load and displacement, an actuation mechanism to accurately perform the prescribed loading profile, and translational stages to precisely position the probe to test regions of interest. Numerous commercial instruments are available, and each achieves these basic instrumentation requirements in different ways. Two examples are given in Figure 8.12. These and other instruments are also described in greater detail in Fischer-Cripps (Fischer-Cripps 2004). Typical noise floors in commercial nanoindenters are sub-nm in displacement and sub-μN in force. Thermal stability and vibration isolation are critical to achieving quality nanoindentation measurements, so nanoindenters are usually housed in their own, specially designed enclosures. For materials sensitive to changes in moisture content, relative humidity also needs to be controlled within the nanoindenter enclosure.

Surface indentation can also be performed with an AFM, which is more sensitive at shallow depths and lower loads than a nanoindenter. During AFM-based indentation, piezo actuation is used to press the AFM tip into the material. The measured deflection of the cantilever is used to assess depth. By estimating the cantilever spring constant, the measured deflection is also used to assess the load. For applications where extremely shallow indentation depths are required, such as in the characterization of individual cellulose nanocrystals (Lahiji et al. 2010), AFM-based indentation is more suitable than conventional nanoindentation. However, uncertainties in probe shape and cantilever spring constant can produce large errors in AFM-based indentation measurements. In addition, the cantilever beam can impart lateral forces to the surface in addition to the usual normal forces, a factor that is not accounted'for in usual nanoindentation analysis.

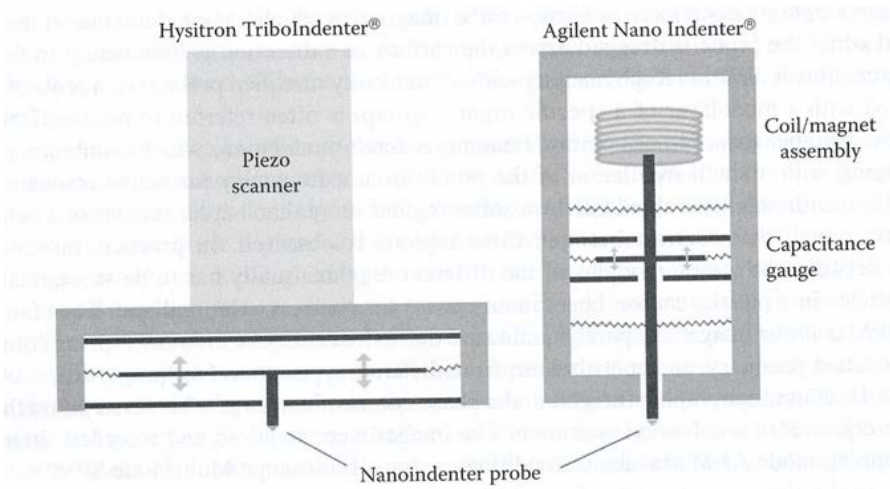

FIGURE 8.12 Two examples of the basic instrumentation used in commercial nanoindenters. The Hysitron Inc. (Minneapolis, MN, USA) TriboIndenter® uses a three plate capacitive force/displacement transducer. The probe is attached to the center plate which is suspended between the two outer plates by leaf springs. To measure displacement, an AC signal 180° out of phase is applied to the two outer plates creating an electric field potential between the two outer plates that is zero in the center. The voltage measured from the middle plate is calibrated to measure displacement. Force is applied to the center plate by applying a large DC offset to the bottom or top plate, which creates an electrostatic attraction with the center plate that can be calibrated as a force. The transducer is attached to a piezo scanner, which allows the nanoindenter probe to also be used as an imaging probe, similar to contact mode AFM. The Agilent (Santa Clara, CA, USA) Nano Indenter® uses an electromagnetic force transducer and capacitance gauge to measure displacement. The probe assembly is also supported by leaf springs.

The size-scale of nanoindentation makes it an ideal tool for many areas of wood science research, including studying both unmodified and modified wood cell walls, adhesives, and coatings. Wimmer and coworkers were the first to use nanoindentation to assess the mechanical properties of S2 cell wall laminae and compound corner middle lamellae in wood (Wimmer and Lucas 1997, Wimmer et al. 1997). They assessed the properties in the longitudinal direction, similar to those shown in Figure 8.13a for loblolly pine *(Pinus taeda)*. The indents were made using a Berkovich probe, a three-sided pyramid commonly used in nanoindentation. Other types of probes, such as cube corner (a three-sided pyramid that is sharper than the Berkovich), conical, spherical, and flat punches, can also be used (Fischer-Cripps 2004). The load-depth traces for the same indents are also shown in Figure 8.13b. They are comprised of three segments: a loading segment, a hold segment at maximum load, and an unloading segment. Accurate depth measurements require accounting for the machine compliance of the nanoindenter. The machine compliance arises from deformation in the instrument itself, such as compression of the shaft connecting the probe to the load actuator. The machine compliance can easily be measured by performing a series of indents with varying loads in a standard material like fused silica and employing the SYS correlation (Stone et al. 1991, Jakes et al. 2008a). Commercial instruments already have built into them the calibration routines that rely on a version of this correlation and can be set up to automatically remove displacement arising from the machine compliance from the depth measurements.

The Oliver—Pharr method (Oliver and Pharr 1992, 2004) is the most common nanoindentation analysis used to calculate Meyer hardness (i.e., load divided by projected area) and elastic modulus. In this method, contact area of the indent is estimated using the contact depth calculated directly from the load-depth trace and a predetermined area function for the probe used in the experiment (Oliver and Pharr 1992, 2004). Therefore, unlike traditional hardness tests, there is no need to image the residual indent impressions to determine the contact area. If necessary, high-resolution images of residual indent impressions, usually obtained from AFM or SEM, can be used to manually measure the contact area. Meyer hardness is a metric of deformation resistance and is usually defined as the maximum load achieved just prior to unloading divided by the contact area of the indent. For highly elastic materials, such as rubber, the Meyer hardness is proportional to the Young's modulus. When yielding takes place beneath the indenter the hardness becomes proportional to flow stress (yield stress at some particular strain, 7-8% for a Berkovich indenter). The proportionality "constant" between hardness and flow stress depends on the hardness/modulus ratio of the material

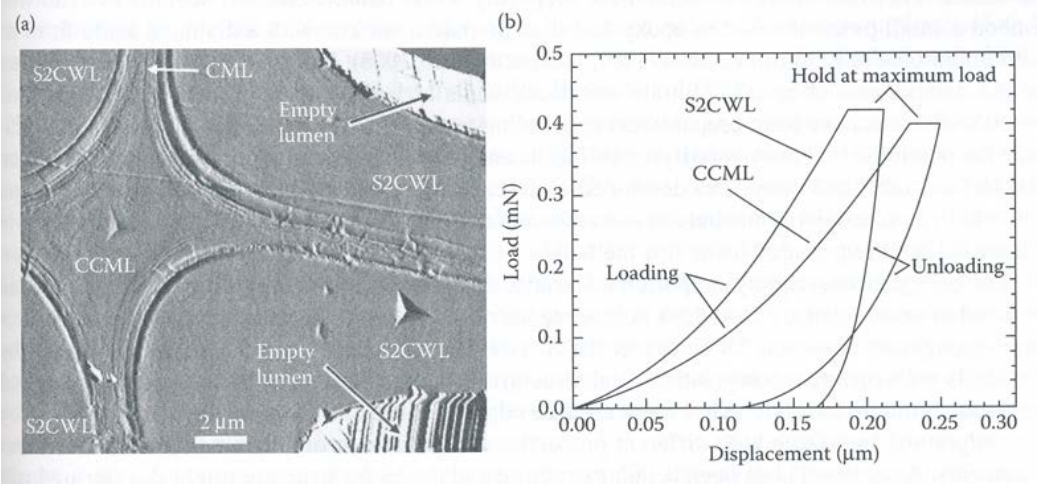

FIGURE 8.13 AFM images (a) of nanoindents placed in the compound corner middle lamella (CCML) and S2 cell wall lamina (S2CWL). The CCML is formed at the junction of three or more tracheids and is part of the compound middle lamella (CML). Load-depth traces (b) of these nanoindents are also shown.

tested (Johnson 1985, Jakes et al. 2011b). Values of 350 and 400 MPa were calculated using the Oliver—Pharr method for the compound corner middle lamella and S2 cell wall lamina, respectively, in Figure 8.13. Elastic modulus is calculated from the initial slope of the unloading segment in a load-depth trace and the contact area. Note that both the indents in Figure 8.13 are approximately the same size, but the initial slope of the unloading segment in the load-depth trace for the compound corner middle lamella is noticeably lower than for the S2 cell wall lamina. This indicates the elastic modulus is lower in the compound corner middle lamella and indeed, for these particular indents elastic moduli of 5 GPa and 18 GPa were calculated using the Oliver—Pharr method for the compound corner middle lamella and S2 cell wall lamina, respectively.

Ever since the pioneering work of Wimmer et al. (Wimmer and Lucas 1997, Wimmer et al. 1997), nanoindentation has been used in many areas of wood science research including mechanical properties of different types of wood cells (Gindl et al. 2002, 2004a, Tze et al. 2007); unmodified wood cell walls from different tree species (Wu et al. 2009, Gershon et al. 2010); wood adhesives and wood-adhesive bond lines (Gindl et al. 2004b,c, Konnerth and Gindl 2006, 2008, Konnerth et al. 2006, 2007, Follrich et al. 2010, Stöckel et al. 2010a,b); cell walls conditioned at different values of relative humidity (Yu et al. 2010); thermally modified cell walls (Stanzl-Tschegg et al. 2009); melamine-modified cell walls (Gindl et al. 2002); pyrolized cell walls (Zickler et al. 2006, Brandt et al. 2010); cell walls damaged in the process of making wood composites (Xing et al. 2009, Gacitua et al. 2010); biologically degraded cell walls (Konnerth et al. 2010b, Lehringer et al. 2011); and bleached pulp fiber cell walls (Adusumalli et al. 2010a). All these studies employed the standard Oliver—Pharr method. Even though the Oliver—Pharr method has provided wood researchers with useful results, the validity and significance of the nanoindentation results has been questioned (Gindl and Schoberl 2004, Jakes et al. 2008a, Jager et al. 2011). Of particular concern are the violations of the basic assumptions of the Oliver—Pharr method. The Oliver—Pharr method assumes the material tested is homogeneous, is rigidly supported in the nanoindenter, and is isotropic. Experiments performed in wood cell walls violate these assumptions. The Oliver—Pharr method also does not address issues associated with testing materials with time-dependent mechanical properties, which wood cell walls possess. Much recent work has focused on overcoming these shortfalls of the standard Oliver—Pharr method to better understand the meaning of nanoindentation results in wood science research. In addition, improved methods for sample preparation have been developed.

Surfaces prepared for nanoindentation must be smooth on the nanometer-scale. Also, the technique used to prepare the surface must not affect the mechanical properties of the material that is to be tested. The most common method for preparing wood nanoindentation specimens is to first embed a small piece of wood in epoxy and then prepare a surface with a diamond knife fit in an ultramicrotome (e.g., Wimmer et al. 1997, Konnerth et al. 2008). However, it is uncertain whether or not components of epoxy infiltrate wood cell walls and affect their properties. Unembedded wood specimens have been prepared using grinding and polishing (Zickler et al. 2006). To eliminate the possibility of epoxy-modifying cell walls and to limit the amount of mechanical damage on the surface, Jakes and coworkers developed a surface preparation method that also uses a diamond knife fit in an ultramicrotome but not any embedment (Jakes et al. 2008a,b, 2009a). The surfaces in Figure 8.13a were prepared using this method.

The homogeneous, rigidly supported material assumptions of the Oliver—Pharr method are often violated in wood science research. A homogeneous material has a consistent composition and structure throughout. However, for instance, the S_2 cell wall lamina (Figure 8.13a), is surrounded by materials with different compositions and structures, such as the S_1 and S_3 cell wall laminae and compound middle lamellae. Also, there are free edges because of the empty lumina. These nearby free edges and interfaces with different properties can produce artifacts in nanoindentation measurements. Also, wood is an open cellular structure and the entire structure might flex during loading, which violates the rigid-support assumption. Jakes and coworkers recently developed the structural compliance method to better understand the effects of edges and specimen-scale flexing in nanoindentation measurements (Jakes et al. 2008a, 2009a). They found that the effect of a nearby

edge or specimen-scale flexing is to introduce a structural compliance into the measurement, which behaves similar to the machine compliance. Therefore, a method similar to the one used to assess the machine compliance, which utilizes the SYS correlation, can be used to assess the structural compliance so its affects can be removed from the measurement. Jakes and Stone also developed expressions predicting the effect of a free edge on hardness and elastic modulus measurements made using the Oliver—Pharr method (Jakes and Stone 2011), which allows researchers to both anticipate the effects of edges and design experiments that minimize edge effects.

The mechanical properties of an isotropic material are the same in all directions. Materials like the compound corner middle lamella and wood adhesives can likely be considered isotropic. However, properties of S_2 cell wall laminae cannot be considered isotropic because mechanical properties, especially elastic modulus, are influenced by the orientation of the stiff cellulose microfibrils. The microfibrils are wound helically around a wood cell and oriented more closely with the longitudinal axis than the transverse axis in a typical wood cell. As a consequence, the longitudinal elastic modulus is higher than the transverse elastic modulus. Because stress fields beneath an indenter are multiaxial, the elastic modulus assessed by nanoindentation will be influenced by the different elastic moduli and fall between the actual longitudinal and transverse elastic moduli. Using previously derived nanoindentation solutions (Vlassak et al. 2003), Jager and coworkers (Jager et al. 2011) developed the relationship between nanoindentation elastic modulus and S_2 cell wall laminae elastic constants assuming transverse isotropy. Using this relationship and experimental nanoindentation elastic moduli from S_2 cell wall laminae tested at different microfibril angles, Konnerth and coworkers (Konnerth et al. 2010a) calculated a longitudinal elastic modulus of 26 GPa and a transverse elastic modulus of 5 GPa for the S_2 cell wall lamina. For comparison, the nanoindentation elastic modulus when the cellulose microfibrils were oriented parallel to the indentation direction was about 18 GPa.

Most materials of interest to wood science, including wood cell walls, adhesives, composite matrices, and coatings, possess time-dependent mechanical properties. A better understanding of these time-dependent material properties would have many benefits in wood science research, such as an improved understanding of the time-dependent properties of bulk wood and wood-based composites. Also, time-dependent properties provide clues into the physical mechanisms that control properties. Not surprisingly, the assessed hardness and elastic modulus measured from nanoindentation depend on the times used in the loading profile (Tang and Ngan 2003, Fujisawa and Swain 2008). For instance, a longer hold segment allows the indenter to penetrate deeper into the material, resulting in a lower Meyer hardness. Therefore, reported property values are not unique and depend on the loading profile used. Numerous approaches have been proposed to better understand and assess time-dependent properties using nanoindentation (e.g., Loubet et al. 2000, Asif et al. 2001, Cheng and Cheng 2004, Vanlandingham et al. 2005, Herbert et al. 2009, Jakes et al. 2011a,b, Oyen 2011). In some approaches, dynamic experiments are performed by superimposing a small sinusoidal signal on the static load, allowing viscoelastic properties such as storage and loss moduli to be assessed over a range of frequencies (Loubet et al. 2000, Asif et al. 2001, Herbert et al. 2009). A common practice in interpreting time-dependent nanoindentation data is to assume a particular material constitutive model and solve the associated contact problem for a given probe geometry (Cheng and Cheng 2004, Vanlandingham et al. 2005, Oyen 2011). One must apply this approach with caution, however, because the results are at best as good as the assumed constitutive model, and many varieties of constitutive model can be used to fit experimental data. A more recent approach to assessing time-dependent properties is the application of broadband nanoindentation (Puthoff et al. 2009, Jakes et al. 2011a,b), in which viscoplastic and viscoelastic properties are independently assessed over a wide range of time-scale (approximately 4-5 orders of magnitude) without need to rely on a specific constitutive model to interpret the results. Broadband nanoindentation creep, which is a viscoplastic measurement, has already been used to better understand the effects on wood cell walls of ethylene glycol plasticization (Jakes et al. 2008b) and polymeric diphenyl diisocyanate adhesive infiltration (Jakes et al. 2009b).

Other modes of nanoindentation testing are also available (Fischer-Cripps 2004). Many commercial instruments are capable of applying a lateral force and measuring lateral displacement, which facilitates scratch testing. Scratch testing is particular useful for understanding scratch resistance in protective coating and investigating substrate-coating interface failures. Nanoindentation probes can also be used as scanning probes to create images, similar to the operation of an AFM. During imaging, a small force, typically 1μN or less, is used to maintain contact with the probe. By applying a small sinusoidal load signal during scanning, elastic modulus maps can be created (Asif et al. 2001). By changing the force applied during probe scanning or changing the number of times an area is scanned, wear testing can be performed. Fracture events during nanoindentation can be investigated by analyzing the associated discontinuities in displacements in load-depth traces, or in some specialized instruments using acoustic emissions. Nanoindenters are also available to perform impact testing. Variable temperature nanoindentation is becoming increasingly common and has been used to study the effects of temperature on wood adhesives (Konnerth and Gindl 2008). Instrumentation is available to combine nanoindentation with SEM, which allows researchers to observe deformation mechanisms as they occur. This technique has been used to study *in situ* deformation of S_2 cell wall laminae (Adusumalli et al. 2010b) and single wood pulp fibers in the transverse direction (Adusumalli et al. 2010c). Instrumentation is also available to perform indentation inside a transmission electron microscope (TEM), which facilitates observation of atomic-scale deformations. However, so far at least, *in situ* TEM nanoindentation has primarily been used in metallurgical research (Minor et al. 2001, De Hosson et al. 2006).

The future of nanoindentation in wood science research holds numerous opportunities. In areas already benefiting from nanoindentation, like understanding effects of wood modifications on cell wall mechanical properties, nanoindentation will continue to aid researchers. In addition to assessing changes in mechanical properties, nanoindentation is also capable of becoming a tool to better understand the mechanisms controlling the properties. By combining techniques to assess properties over a wide range of time-scale, particularly broadband nanoindentation (Jakes et al. 2011a,b), with variable temperature or variable relative humidity capabilities, nanoindentation is transformed into a localized tool for mechanical spectroscopy. The kinetic signatures arising from mechanical spectroscopy results can be analyzed to gain insight into the physical mechanisms controlling the properties. *In situ* TEM indentation presents researchers with the exciting possibility to actually observe these mechanisms while they are occurring. Another exciting possibility is combining indentation with spectroscopic techniques, which gives the opportunity to observe changes in polymer chemistry or orientation during deformation beneath an indenter.

8.3 SPECTROSCOPIC METHODS FOR CHARACTERIZING SURFACE PROPERTIES

Although a broad array of spectroscopic methods for surface analysis of materials exists, only a handful of these have been applied in the characterization of wood surfaces. The focus of this section will be on those methods that the author deemed to be of greatest interest.

Spectroscopic methods may be divided into three classes: molecular, electronic, and mass spectroscopies. Molecular spectroscopy includes Fourier transform infrared (FTIR), Fourier transform attenuated total reflectance infrared (FT—ATR), and Fourier transform Raman (FT-Raman) methods. Electronic spectroscopy includes x-ray photoelectron (XPS), and energy dispersive x-ray spectroscopy (EDXA, EDX, or EDS). Mass spectroscopy includes secondary ion mass spectroscop (SIMS) and static secondary ion mass spectroscopy (SSIMS).

8.3.1 MOLECULAR SPECTROSCOPY

Molecular spectroscopic methods can provide information about the chemical composition of a surface. However, successful characterization of a wood surface by any of the molecular spectroscopi

techniques depends upon judicious choice of sampling techniques and critical interpretation of the data. Detailed descriptions of the fundamentals and application of molecular spectroscopy have been given elsewhere (Mirabella 1998, Stuart 2004). As significant advances in instrumentation are realized, new applications of infrared spectroscopy in surface characterization of wood have emerged.

FTIR and FT—ATR spectra of wood samples have been reported in the literature (Deshmukh and Aydil 1996, Tshabalala et al. 2003). Assignment of infrared absorption bands measured by different FTIR techniques is given in Table 8.1. Figure 8.14 shows examples of infrared spectra of the surface of a softwood wafer obtained by FTIR—ATR.

Infrared analysis of wood surfaces is generally not considered to be sufficiently surface sensitive because the sampling depth of infrared radiation is of the order of 100 gm. Consequently changes in infrared spectral features due to changes in surface chemistry are often masked by the spectral features of the underlying bulk chemistry of the wood specimen. In the example shown in Figure 8.14b, the peaks at 2916, 2847, 1269, 894, and 769 cm-^{1} were attributed to the alkoxysilane thin film that was deposited on the wood wafer (Tshabalala et al. 2003). The peaks at 2916 and 2847 cm^{-1} were assigned to the asymmetric and symmetric C—H stretch modes of the —CH_3 and —CH_2 groups (Sahli et al. 1994, Deshmukh and Aydil 1996, Conley 1996); the peak at 1269 cm^{-1} was assigned to the Si—CH_3 bending mode; and the peaks at 894 and 769 cm^{-1} were assigned to Si—C, Si—O, and

TABLE 8.1
Assignment of IR Bands of Solid Wood or Wood Particles Measured by Diffuse Reflectance FTIR

Band Position (cm^{-1})	Assignment
3380 (3418)a	O—H stretch vibration (bonded)
2928 (2928)	C—H stretch vibration
1736 (1745)	C=O stretch vibration (unconjugated)
1655 (1660)	H—O—H deformation vibration of adsorbed water and conjugated C=O stretch vibration
1595 (1596)	Aromatic skeletal and C=O stretch vibration
1504 (1507)	Aromatic skeletal vibration
1459 (1465)	C—H deformation (asymmetric) and aromatic vibration in lignin
1423 (1427)	C—H deformation (asymmetric)
1372 (1374)	C—H deformation (symmetric)
1326 (1329)	—CH_2 wagging vibration in cellulose
1267 (1270)	C-O stretch vibration in lignin, acetyl, and carboxylic vibration in xylan
1236 (1242)	C-O stretch vibration in lignin, acetyl, and carboxylic vibration in xylan
1158 (1165)	C-O—C asymmetric stretch vibration in cellulose and hemicellulose
1113 (1128[b])	O—H association band in cellulose and hemicellulose
1055[b] (1083)	C-O stretch in cellulose and hemicellulose
1042 (1036)	C-O stretch
1000 (1003)	C-O stretch in cellulose and hemicellulose
897 (899)	Cl group frequency in cellulose and hemicellulose
667 (670)	C-O—H out-of-plane bending mode in cellulose

Source: Adapted from Pandey, K.K. and Theagarajan, K.S. 1997. *Holz als Roh- and Werkstoff* 55:383-390.

[a] Quantities given in parenthesis correspond to band positions obtained from solid wood chips or wood particles undiluted with KBr.

[b] Highest intensity band.

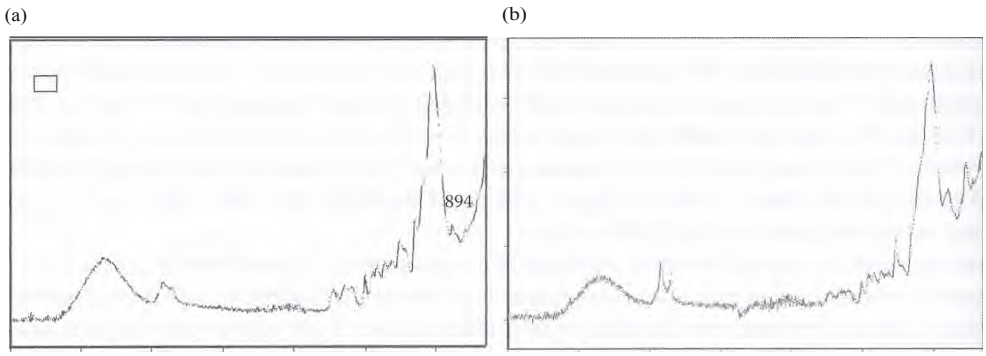

FIGURE 8.14 FTIR—ATR spectra of a wood wafer before (a) and after (b) coating with a thin film of alkoxysilanes.

Si—O—CH_3 groups (Selamoglu et al. 1989, Fracassi et al. 1992, Libermann and Lichtenberg 1994, Conley 1996).

Raman and infrared spectra give basically the same kind of molecular information, and both methods can be used to supplement or complement each other. Although Raman spectra are theoretically simpler than the corresponding infrared spectra, primarily because overlapping bands are much less common in Raman spectroscopy, its use in the study of wood surfaces is not widespread. The primary reason for this lack of popularity has been the difficulty of obtaining sufficiently intense Raman bands, which are not completely masked by the fluorescence bands emitted by the wood components when irradiated with visible light. However, with the advent of FT-Raman and introduction of the red laser source (excitation wavelength, 1064 nm), this difficulty has been largely overcome, and application of FT-Raman to the study of wood surfaces is likely to increase.

FT-Raman spectra of wood and wood components have been reported in the literature (Agarwal and Ralph 1997, Agarwal 1999). Table 8.2 gives a summary of band assignment in the FT-Raman spectra of wood components.

8.3.2 ELECTRON SPECTROSCOPY

Electron spectroscopy is concerned with the energy analysis of low energy electrons (generally in the range of 20-2000 eV) liberated from the surface of a specimen when it is irradiated with soft x-rays or bombarded with an electron beam (Watts 1990). Two methods of electron spectroscopy have been developed; x-ray photoelectron spectroscopy (XPS), also known as electron spectroscopy for chemical analysis (ESCA); and Auger electron spectroscopy (AES). Since AES has not been applied to the study of wood surfaces, the rest of this discussion will focus on XPS, which has been widely used for the characterization of the elemental composition of wood surfaces.

In XPS, the surface of a sample maintained in a high vacuum (10^{-6}-10^{-11} torr) is irradiated with x-rays, usually from Mg or Al anodes, which provide photons of 1253.6 eV and 1486.6 eV, respectively. Electrons are ejected from the core levels of atoms in the surface, and their characteristic binding energies are determined from the kinetic energy of the ejected electrons and the energy of the incident x-ray beam.

The kinetic energy (E_K) of the electron is the experimental quantity measured by the spectrometer. The binding energy of the electron (E_B) is related to the experimentally measured kinetic energy by the following relationship:

$$E_B = h\nu - E_K - W \tag{8.1}$$

where $h\nu$ is the incident photon energy and W is the spectrometer work function.

TABLE 8.2
Raman Band Assignment in the Spectra of Softwood Cellulose and Lignin

Band Position (cm^{-1})	Assignment	Attributed to
3065 ma	Aromatic stretch	Lignin
3007 sh	C—H stretch in OCH_3, asymmetric	Lignin
2938 m	C—H stretch in OCH_3, asymmetric	Lignin
2895 vs	C—H and CH_2 stretch	Cellulose
2886 sh	C—H stretch in R_3C—H	Lignin
2848 sh	C—H and CH_2 stretch	Cellulose
2843 m	C—H stretch in OCH_3, symmetric	Lignin
1658 s	Ring conj. C=C stretch of coniferyl alcohol; C=O stretch of coniferylaldehyde	Lignin
1620 sh	Ring conjugated C=C stretch of coniferylaldehyde	Lignin
1602 vs	Aryl ring stretch, symmetric	Lignin
1508 vw	Aryl ring stretch, asymmetric	Lignin
1456 m	H—C—H and H—O—C bending	Cellulose
1454 m	O—CH_3 deformation; CH_2 scissoring; guaiacyl ring vibration	Lignin
1428 w	O—CH_3 deformation; CH_2 scissoring; guaiacyl ring vibration	Lignin
1393 sh	Phenolic O—H bend	Lignin
1377 m	H—C—C, H—C-O, and H—O—C bending	Cellulose
1363 sh	C-H bend in R_3C—H	Lignin
1333 m	Aliphatic O—H bend	Lignin
1298 sh	H—C—C and H—C-O bending	Cellulose
1297 sh	Aryl-O of aryl-OH and aryl-O-CH_3; C=C stretch of coniferyl alcohol	Lignin
1271 m	Aryl-O of aryl-OH and aryl-O-CH_3; guaiacyl ring (with C=O group)	Lignin
1216 vw	Aryl-O of aryl-OH and aryl-O-CH_3; guaiacyl ring (with C=O group)	Lignin
1191 w	A phenol mode	Lignin
1149 sh	C—C and C-O stretch plus H—C—C and H—C-O bending	Cellulose
1134 m	A mode of coniferaldehyde	Lignin
1123 s	C—C and C-O stretch	Cellulose
1102 w	Out of phase C—C-O stretch of phenol	Lignin
1095 s	C—C and C-O stretch	Cellulose
1073 sh	C—C and C-O stretch	Cellulose
1063 sh	C—C and C-O stretch	Cellulose
1037 sh	C—C and C-O stretch	Cellulose
1033 w	C-O of ary1-O-CH_3 and aryl-OH	Lignin
1000 vw	C—C and C-O stretch	Cellulose
971 vw	C—C and C-O stretch	Cellulose
969 vw	—C—C—H and —HC = CH— deformation	Lignin
926 vw	—C—C—H wag	Lignin
900 vw	Skeletal deformation of aromatic rings, substituent groups, and side chains	Lignin
899 m	H—C—C and H—C—O bending at C6	Cellulose
787 w	Skeletal deformation of aromatic rings, substituent groups, and side chains	Lignin
731 w	Skeletal deformation of aromatic rings, substituent groups, and side chains	Lignin

continued

TABLE 8.2 (continued)
Raman Band Assignment in the Spectra of Softwood Cellulose and Lignin

Band Position (cm^{-1})	Assignment	Attributed to
634 vw	Skeletal deformation of aromatic rings, substituent groups, and side chains	Lignin
591 vw	Skeletal deformation of aromatic rings, substituent groups, and side chains	Lignin
555 vw	Skeletal deformation of aromatic rings, substituent groups, and side chains	lignin
537 vw	Skeletal deformation of aromatic rings, substituent groups, and side chains	Lignin
520 m	Some heavy atom stretch	Cellulose
491 vw	Skeletal deformation of aromatic rings, substituent groups, and side chains	Lignin
463 vw	Skeletal deformation of aromatic rings, substituent groups, and side chains	Lignin
458 m	Some heavy atom stretch	Cellulose
435 m	Some heavy atom stretch	Cellulose
384 w	Skeletal deformation of aromatic rings, substituent groups, and side chains	Lignin
380 m	Some heavy atom stretch	Cellulose
357 w	Skeletal deformation of aromatic rings, substituent groups, and side chains	Lignin
351 w	Some heavy atom stretch	Cellulose

Source: Adapted from Agarwal, U.P. 1999. In: *Advances in Lignocellulosic Characterization.* Dimitris S. Argyropoulos (ed.), TAPPI Press, Atlanta, Georgia.

[a] *Note:* vs = very strong; s = strong; m = medium; w = weak; vw = very weak; sh = shoulder. Band intensities are relative to other peaks in the spectrum.

The kinetic energy of the electrons ejected from the surface of a specimen is determined by means of an analyzer, which gives a photoelectron spectrum. The photoelectron spectrum gives an accurate representation of the electronic structure of an element, as all electrons with a binding energy less than the incident photon energy will be featured in the spectrum.

The characteristic binding energy of a given atom is also influenced by its chemical environment. This dependence allows the assignment of a given atom to a particular chemical functional group on the surface. The sampling depth of XPS is about 5-10 nm.

Examples of survey and high-resolution XPS spectra of a wood specimen are shown in Figures 8.15 and 8.16 respectively. The survey spectrum gives the surface elemental composition of the wood specimen. As expected the spectrum is dominated by carbon and oxygen peaks, which are the elements that make up the constituents of wood. The high-resolution spectrum of the carbon peak shows the presence of different chemical states or classes of carbon on the wood surface.

In early pioneering studies on the surface analysis of paper and wood fibers by XPS, Cls, and Ols spectra were obtained for samples of WhatmanTM filter paper, bleached kraft and bleached sulfite paper, spruce dioxane lignin, stone groundwood pulp, refiner mechanical pulp and thermo-mechanical pulp.

The Cls peak was observed to consist of four main components, which were ascribed to four classes of carbon atoms present in wood components. Class-I carbon atoms are those bonded to carbon or hydrogen; Class-II carbon atoms are bonded to a single noncarbonyl oxygen atom; Class-III carbon atoms are bonded to two noncarbonyl atoms or to a single carbonyl oxygen atom;

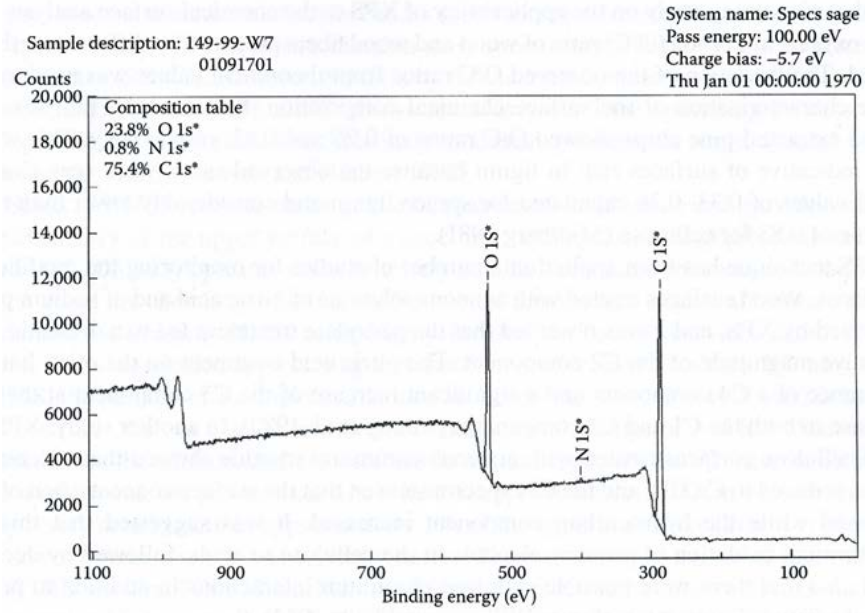

FIGURE 8.15 XPS survey spectrum of a wood specimen of *Pinus taeda* shows the elemental composition of the surface.

and Class-IV carbon atoms are ascribed to the carboxyl carbon. The four components were designated Cl, C2, C3, and C4 respectively. The change in the relative magnitude of these components as a function of the oxygen ratio was taken to suggest that both lignin and extractives contribute to the change in surface composition on going from pure cellulose to mechanical wood pulps (Dorris and Gray 1978a,b, Gray 1978).

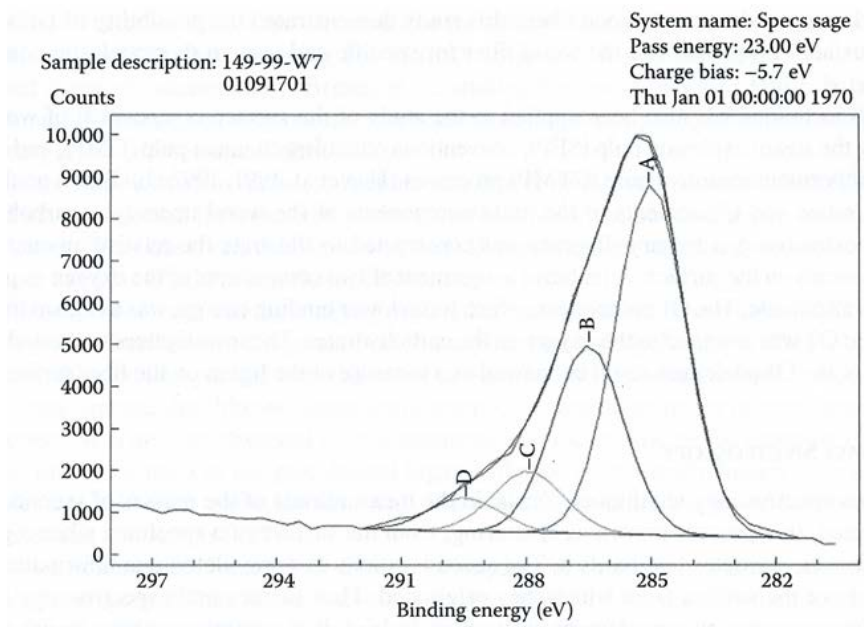

FIGURE 8.16 High-resolution XPS spectrum of the Cl_s. carbon showing the existence of different states or classes of carbon atoms on the surface of the wood specimen (A = Cl; B= C2; C= C3; and D = C4).

In another pioneering study on the applicability of XPS to the chemical surface analysis of wood fibers, the oxygen-to-carbon (0/C) ratio of wood and wood fibers prepared by different methods was determined The deviation of the observed 0/C ratios from theoretical values was used to provide qualitative characterization of the surface chemical composition. For example, samples of unextracted and extracted pine chips showed 0/C ratios of 0.26 and 0.42, respectively. This was interpreted as indicative of surfaces rich in lignin because the observed ratios were very close to the theoretical values of 0.33-0.36 calculated for spruce lignin and considerably lower than the theoretical value of 0.83 for cellulose (Mjorberg 1981).

The XPS technique has been applied in a number of studies for monitoring the modification of wood surfaces. Wood surfaces treated with aqueous solutions of nitric acid and of sodium periodate were analyzed by XPS, and it was observed that the periodate treatment led to a dramatic increase in the relative magnitude of the C2 component. The nitric acid treatment on the other hand led to the appearance of a C4 component and a significant increase of the C3 component at the expense of a decrease in both the Cl and C2 components (Young et al. 1982). In another study, XPS data of wood and cellulose surfaces treated with aqueous chromium trioxide showed that at least 75% of Cr(VI) was reduced to Cr(III), and the C1s spectra showed that the surface concentration of hydroxyls decreased while the hydrocarbon component increased. It was suggested that this change occurred through oxidation of primary alcohols in the cellulose to acids, followed by decarboxylation, and also that there were possible cellulose-chromium interactions in addition to previously proposed chromium-lignin interactions (Williams and Feist 1984).

Changes in the surface chemical composition of solid residues of quaking aspen *(Populus tremuloides)* wood extracted with supercritical fluid methanol were monitored by XPS, and it was shown that the C1s peak provided information that allowed for the rapid measurement of the proportion of carbon in polyaromatics. The components of the 01 s peak were also tentatively assigned to oxygen in the major wood components, and to minor extractives, recondensed material and strongly adsorbed water (Ahmed et al. 1987, 1988). In another XPS study of weathered and UV-irradiated wood surfaces, the observed increase in the 0/C ratio was interpreted as an indication of a surface rich in cellulose and poor in lignin (Hon 1984, Hon and Feist 1986).

The surface composition of grafted wood fibers has also been characterized by XPS. By grafting poly(methyl methacrylate) onto wood fibers this study demonstrated the possibility of tailoring the chemical surface composition of the wood fiber for specific end uses in thermoplastic composites (Kamdem et al. 1991).

The XPS technique has also been applied to the study of the surface composition of wood pulp prepared by the steam explosion pulp (SEP), conventional chemimechanical pulp (CMP), and conventional chemithermomechanical pulp (CTMP) processes (Hua et al. 1991, 1993a,b). Based on the theoretical 0/C ratios and Cl contents of the main components of the wood fibers (i.e., carbohydrates, lignin, and extractives), a ternary diagram was constructed to illustrate the relative amounts of the three components on the surface. A tentative assignment of two components of the oxygen is peak, 01 and 02 was also made. The 01 component, which has a lower binding energy, was assigned to oxygen in lignin, and 02 was assigned to the oxygen in the carbohydrates. The investigators suggested that the percentage of the 01 peak area could be viewed as a measure of the lignin on the fiber surface.

8.3.3 MASS SPECTROSCOPY

Surface mass spectroscopy techniques consist in the measurement of the masses of secondary ions that are ejected, in a process known as sputtering, from the surface of a specimen when a primary beam of energetic particles bombards it. The secondary ions can provide unique information about the chemistry of the surface from which they originated. Thus surface mass spectroscopy and surface electron spectroscopy complement each other. Indeed, it is common practice to use electron spectroscopy in combination with surface mass spectroscopy to characterize the surface chemistry of an unknown specimen (Perry and Somorjai 1994).

There are three main methods of surface mass spectroscopy that are commonly used; secondary ion mass spectrometry (SIMS); laser ionization mass spectrometry (LIMA); and sputtered neutral mass spectrometry (SNMS). However, SIMS is by far the most commonly used of the surface mass spectroscopic techniques. While SIMS always revolves around the sputtering process, different modes of operation of SIMS exist. The three main modes of operation are static, dynamic, and scanning (or imaging) SIMS (Johnson and Hibbert 1992).

Static SIMS (SSIMS) operates under gentle bombardment conditions, and provides information about the chemistry of the upper surface of a specimen, while causing negligible surface damage. Dynamic SIMS (DSIMS) operates under relatively harsher bombardment conditions, and provides information about the chemistry of a surface from a few nanometers to several hundred microns in depth. Scanning or imaging SIMS, using highly focused ion beams, provides detailed chemical images with spatial resolution approaching that associated with SEM (less than 100 nm).

In SSIMS, the surface of a sample maintained in a high vacuum (10^{-6}-10^{-}n torr) is bombarded with ions (Ar+, Xe+, Cs+, or Gal at well-defined energies in the range of 1-4 KeV. Secondary ions are sputtered from the surface, and are detected in a mass spectrometer. To keep depletion of the surface at a minimum, the primary current is held at approximately 1 nA/cm^2. Under these conditions, only a very small fraction, approximately 1%, of the uppermost monolayer is consumed. The relatively low secondary ion flux is typically detected and analyzed in a time-of-flight mass spectrometer (TOFMS). The TOFMS has high sensitivity; extended mass range and high mass resolution, and is applicable to virtually all fields of science and technology where solid surfaces and their behavior are important (Watts 1992, Winograd 1993, Benninghoven et al. 1993, Comyn 1993, Li and Gardella 1994).

The development of SIMS and its application in the study of paper surfaces is the subject of an excellent review by Detter-Hoskin and Busch (1995). Although SSIMS spectra are complicated and sometimes difficult to interpret, the SSIMS technique has been successfully applied in the study of the surface composition and topochemistry of paper surfaces. Brinen compared the information content of XPS and SSIMS for characterizing sized-paper surfaces. He observed that while XPS readily detected the presence of sizing agents, it provided little structural information. Time-of-flight secondary ion mass spectroscopy (ToF—SSIMS) on the other hand, could be used to identify the chemical structures. Brinen also showed that the spatial distribution of the sizing agents on the paper surfaces could be obtained using ToF—SSIMS (Brinen 1993). In a combination of XPS, ToF-SIMS, and paper chromatography, Brinen et al. studied the cause of sizing difficulties in sulfite paper. Using SIMS imaging, they observed concentrated islands of pitch, which were implicated in the desizing effect (Brinen and Kulick 1995).

In another study of paper surfaces, Pachuta and Staral demonstrated that ToF—SSIMS with its extended mass range and high sensitivity was a useful tool for the nondestructive analysis of colorants on paper. They observed that the use of SSIMS conditions produced no detectable alteration of the paper samples (Pachuta and Staral 1994).

SIMS has also been used in the imaging of fiber surfaces. Tan and Reeve used SIMS imaging to reveal the microdistribution of organochlorine on fully bleached pulp fibers. They observed that pulp-bound chlorine was present over the entire surface and throughout the fiber cross-section. On the fiber outer surface, the chlorine concentration was observed to be higher in some small areas. In cross-section, chlorine was observed to be concentrated in the middle of the secondary wall. They concluded that since most of the pulp-bound organochlorine is covalently linked to large carbohydrate molecules held deep within the fiber wall, it was not likely to diffuse out of the fiber even after a long time (Tan and Reeve 1992).

Wang and Peltonen 2011 used ToF—SIMS to compare the surface chemistries of pine sapwood and heat-treated spruce. They found that less oleic, arachidic acid/tripalmitin and triolein and more stearic, behenic acid and sitosterols/sterylester were present on the surface of heat-treated spruce surface compared with pine sapwood. The ToF—SIMS spectra and images were obtained with a PHI TRIFT II instrument (Physical Electronics, USA) using a 15 kV pulsed liquid-metal ion source

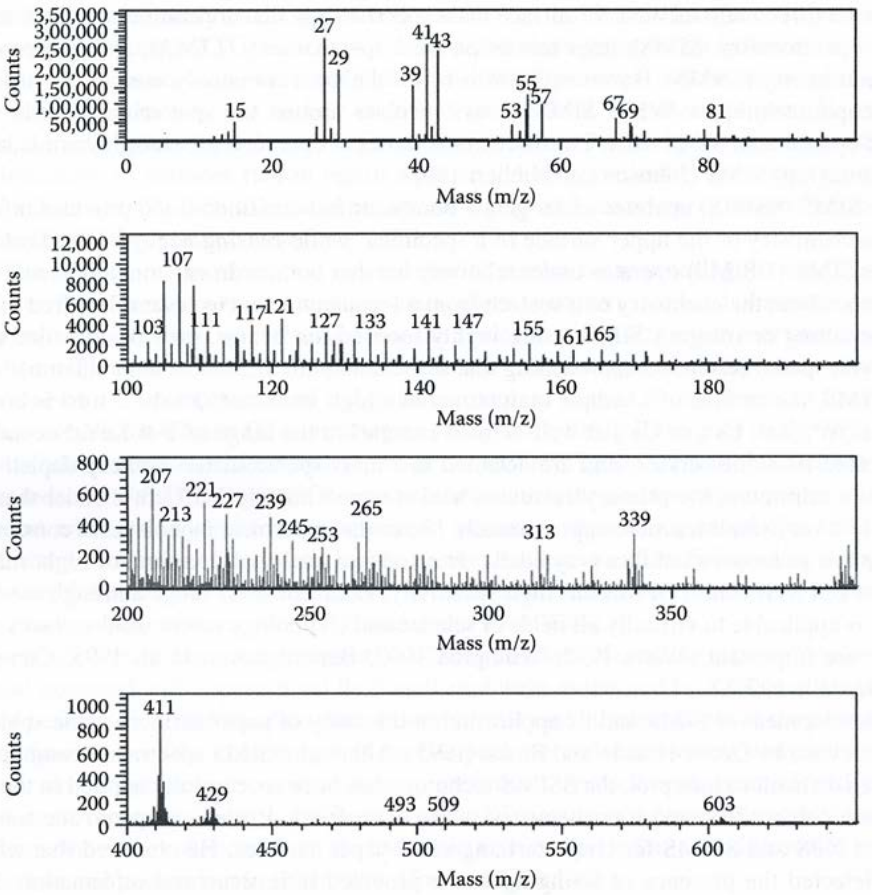

FIGURE 8.17 ToF—SIMS positive ion spectra (m/z = 0-650 amu) for pine sapwood.

(LMIS) enriched in $^{69}Ga+$ ions. The images were obtained using a primary beam of $^{69}Ga+$ LMIS with kinetic energy of 25 keV and operated in the microprobe mode. The raster size was 200 x 200 gm. Images were acquired for 10 min. The charge compensation was performed using an electron flood gun pulsed out-of-phase with the ion gun. The positive ToF—SIMS spectra of pine sapwood and heat-treated spruce (Thermo-S) are shown in Figures 8.17 and 8.18. All the spectral peaks used in the analysis are summarized in Table 8.3. The spectra are shown for mass to charge ratios (m/z) from 0 to 650. For wood samples, mostly fragments of hydrocarbons can be seen in the mass range below 100 m/z (CH_2, CH_3, C_2H_5, and so on). Peaks representing different functionalities in the wood components (e.g., HO-, H_3CO-, and -COO-) can also be seen in this region. However, the compounds or fragments mentioned above are very common in many organic materials, so this region is not discussed in this text. The region from 100-200 m/z was found to be the most interesting spectral range for detecting the molecular fragments of lignin and carbohydrates (Kangas 2007), In the spectra of both pine sapwood and heat-treated spruce (Figure 8.17), the dominant peaks of spruce lignin can be seen at 107 and 121 m/z. These peaks represent the p-hydroxyphenyl units in lignin. However, the intensities of peaks representing guaiacyl at 151, 167 m/z and syringyl units at 167, 181 m/z are relatively weak. The peaks at 115 and 133 m/z originated from xylan, while the peaks at 127 and 145 m/z were interpreted to originate from cellulose. The spectral region of 100-200 m/z for pine sapwood is similar to that of heat-treated spruce. Peaks characteristic of wood extractives are usually seen in the mass to charge ratio from 230 m/z to 650 m/z. In the pine

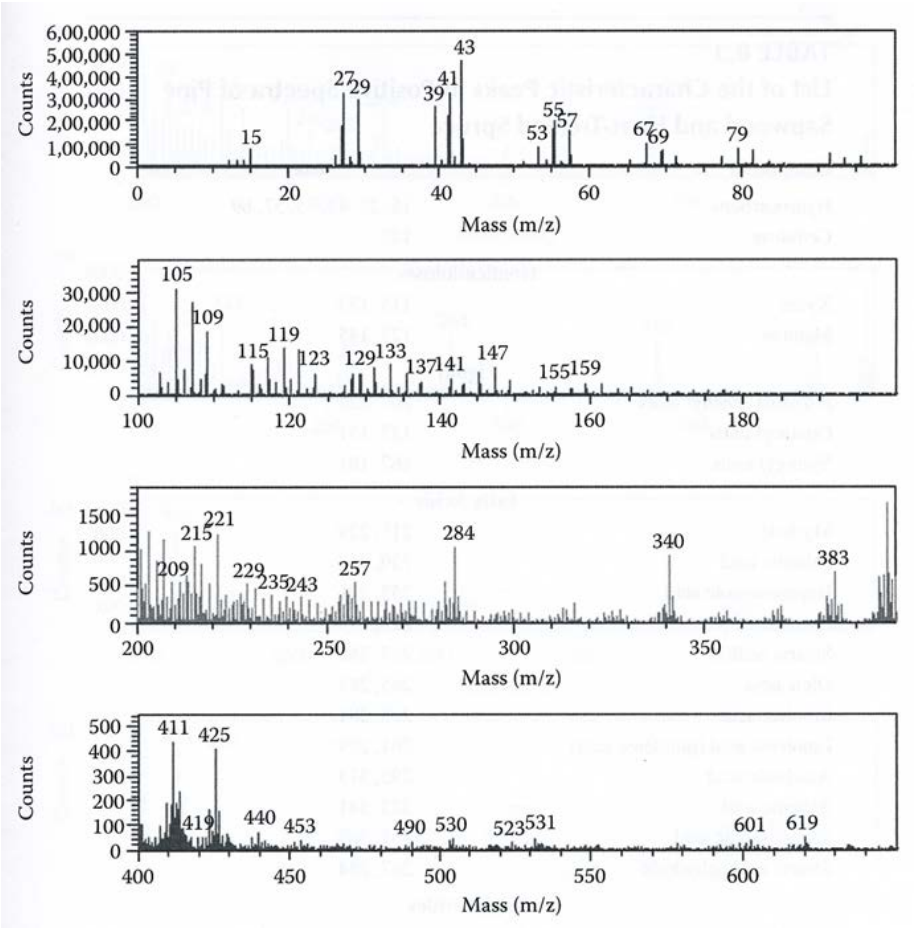

FIGURE 8.18 ToF—SIMS positive ion spectra (m/z = 0-650 amu) for heat-treated spruce (Thermo-S).

sapwood positive spectra, the presence of peaks at around 600 m/z and at 339 m/z indicates that the sample contained triglycerides. In addition, the peaks at 239 m/z originated from palmitic acid, the peak at 253 m/z was assigned to heptadecanoic acid and the peak at 265 m/z was identified as oleic acid. The peak at 313 m/z originated from arachidic acid/tripalmitin. The peaks at 411, 429 m/z originating from steryl ester were also observed in pine sapwood positive spectra. However, with respect to the extractive region for heat-treated spruce, it was seen that the most dominant peaks were those of sterol and steroid (383, 397, 411, 425 m/z) and probably stearic (284 m/z) and behenic acid anhydride (340 m/z), in addition to palmitic acid (239, 257 m/z). In order to obtain semiquantitative information about the surface compounds, the peaks of interest shown in Table 8.3 were integrated and normalized to the total intensity of the spectrum. As shown in Figure 8.19, it is interesting to note that, in comparison with pine sapwood, less oleic, arachidic acid/tripalmitin, and triolein but more stearic acid and sitosterols/sterylester were found on heat-treated spruce surface. This was probably due to some de-esterification of fats and waxes and the migration of extractives such as resins with subsequent degradation during heat treatment of spruce (Sundqvist 2004, Viitaneimi et al. 2001).

SIMS spectral libraries are still at the early stages of development, and as more spectra of biological materials, including lignocellulosic materials are added to the libraries, SIMS will become a very productive technique for characterizing the surface chemistry of wood and wood composites.

TABLE 8.3
List of the Characteristic Peaks in Positive Spectra of Pine Sapwood and Heat-Treated Spruce

Compound	Peaks
Hydrocarbons	15, 27, 41, 55, 57, 69
Cellulose	127
Hemicelluloses	
Xylan	115, 133
Mannan	127, 145
Lignin	
p-hydroxyphenyl units	107,121
Guaiacyl units	137,151
Syringyl units	167,181
Fatty Acids	
Myristic	211, 229
Palmitic acid	239, 257
Heptadecanoic acid	253, 271
Pentadecanoic	225, 243
Stearic acid	267, 285
Oleic acid	265, 283
Linoleic acid	263, 281
Linolenic acid (pinolenic acid)	261, 279
Arachidic acid	295, 313
Behenic acid	323, 341
Tetracosanoic acid	351, 369
Stearic acid anhydride	267, 284
Triglycerides	
Tripalmitin	313, 551
Triolein	339, 603
Tristearin	341, 607
Triglycerides of other fatty acids	327, 335, 337, 575, 595, 599, 600, 601, 602
Resin Acids	
Dehydroabietic acid	299, 399, 301, 302, 303
Abietic acid	299, 300, 301, 302, 303
Steroids	
Ultrasitosterol	383, 397, 414, 429
Steryl esters	383, 397, 411, 412, 425/429
Sterols	
Sitosterol	397, 414, 415
Sitostanol	398, 416
Oxo-sitosterol	411, 429

Source: Adapted from Kangas H. 2007. Surface chemical and morphological properties of mechanical pulps, fibers and fines, November, KCL Communications 13; Fardim P. et al. 2005. *Engineering Aspects* 255:91-103; Tokareva E. 2011. *Doctoral thesis - "Spatial Distribution of Components in Wood by ToF-SIMS".* Åbo Akademi University, Turku.

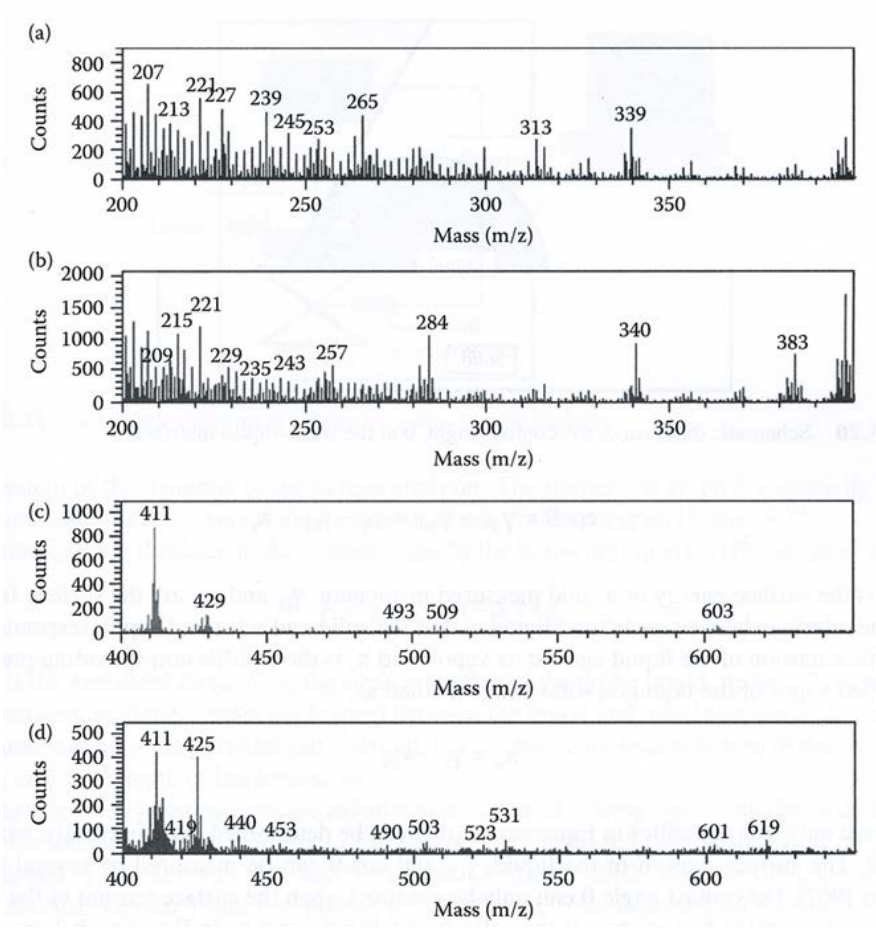

FIGURE 8.19 ToF—SIMS positive ion spectra (m/z = 200-650 amu) for pine sapwood (a, c) heat-treated spruce (b, d).

8.4 THERMODYNAMIC METHODS FOR CHARACTERIZING SURFACE PROPERTIES

Over the years, two methods for determining the surface thermodynamic properties (surface energy and acid-base characteristics) of wood have been developed. The first method, which is known as contact angle analysis (CAA), is based on wetting the wood surface with a liquid. The second technique, which is known as inverse gas chromatography (IGC), is based on the adsorption of organic vapors on the wood surface. Another major difference between the two methods is that solid samples for IGC analysis should be in a finely divided form, while samples for CAA can be in any form, including small coupons or wafers.

8.4.1 CONTACT ANGLE ANALYSIS (CAA)

There are two approaches to CAA: static and dynamic contact angle measurements. In static CAA the liquid—solid angle of a sessile drop of liquid on the surface of a wood specimen is observed and measured by means of a contact angle meter. The contact angle, 0 of a drop of liquid on the surface of a specimen is shown schematically in Figure 8.20. The cosine of the contact angle (cos 0) is related to the surface energy of the specimen by the Young equation (Nguyen and Johns 1978).

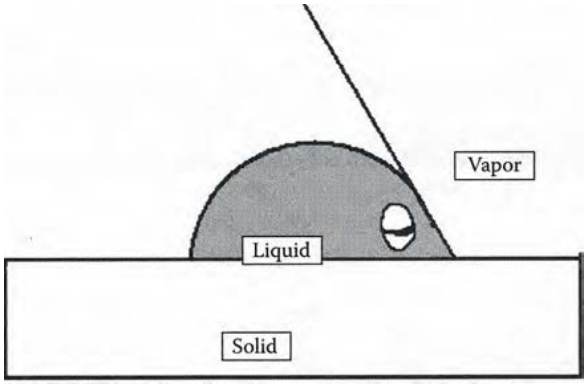

FIGURE 8.20 Schematic diagram of the contact angle, θ at the solid—liquid interface.

$$\gamma_{LV}\cos\theta = \gamma_{SV} - \gamma_{SL} = \gamma_S - \gamma_{SL} - \pi_e$$

where γ_s is the surface energy of a solid measured in vacuum, γ_{SL} and γ_{SV} are the surface free energies on the interface between solid and liquid and of the solid and saturated vapor, respectively; γ_{LV} is the surface tension of the liquid against its vapor, and π_e is the equilibrium spreading pressure of the adsorbed vapor of the liquid on solid and is defined as:

$$\pi_e = \gamma_S - \gamma_{SV} \tag{8.3}$$

There are only two quantities in Equation 8.2 that can be determined experimentally, namely $y_{b,,}$ and cos 0. The surface tension of the liquid, γ_{LV} and cos θ can be measured by several methods (Adamson 1967), but contact angle θ can only be obtained when the surface tension of the liquid is higher than the surface-free energy of the solid (assuming γ_{SL} and π_e in Equation 8.2 are approximately equal to zero). In that case, the surface energy of the solid can be estimated from Equation 8.4:

$$\gamma_S \cong \gamma_{LV}\cos\theta \tag{8.4}$$

Zisman (Adamson 1967) introduced the well-known empirical approach to estimate the surface-free energy of a solid by plotting the cosine of contact angle θ versus the surface tension of a series of liquids of known surface tension. The point at which the resulting straight line plot intercepts the horizontal line, cos θ = 1 (zero contact angle) is called the critical surface tension, γ_C. Zisman's plot is generally described by Equation 8.5.

$$\cos\theta = 1 + b(\gamma_C - \gamma_{LV}) \tag{8.5}$$

where *b* is the slope of the line. Zisman's critical surface tension provides one of the most convenient means of expressing the surface energy of a solid.

In dynamic CAA, the contact angle is measured by means of a dynamic contact angle analyzer (DCA), which consists of a precision balance for measuring the wetting force exerted on a specimen as it is dipped and withdrawn from a liquid of known surface tension, γ_{LV}. As shown in the schematic diagram in Figure 8.21, the weight of the solid specimen is recorded by means of a precision balance as it is immersed and withdrawn from the liquid. Immersion and withdrawal of the specimen is accomplished by raising or lowering the liquid in the cup placed on motorized elevator. The immersion graph, which is also known as a hysteresis loop is captured by a data system that is interfaced to the

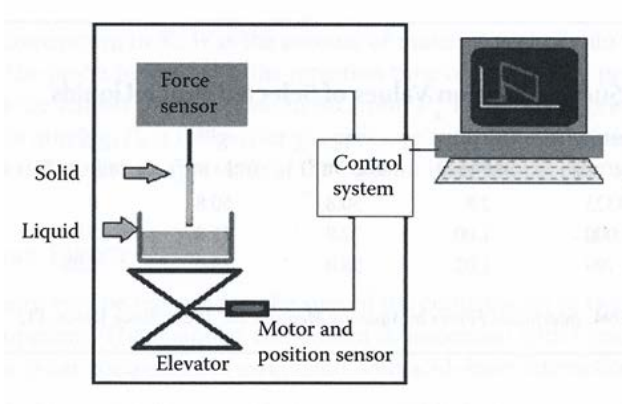

FIGURE 8.21 Schematic diagram of a dynamic contact angle analyzer.

control system of the dynamic contact angle analyzer. The immersion graph is essentially a plot of the measured wetting force versus the immersion depth of the specimen (Figure 8.22).

The wetting force is related to the contact angle by the following equation (De Meijer et al. 2000):

$$F = \gamma_L P \cos\theta - \rho_L g A d \tag{8.6}$$

where F is the measured force, *N;* IL the surface tension of the probe liquid, mJ/m^2; P the perimeter of the specimen, m; 0 the contact angle (deg) between the liquid and wood specimen; ρ_L the density of the liquid, kg/m^3; g the gravitational constant, m^2/s; A the cross-sectional area of the wood specimen, m^2; and d the depth of immersion, *m.*

The surface energy components are calculated from the advancing contact angles of diiodomethane, formamide, and water according to Equations 8.2 through 8.5, which are based on Equation 8.3, developed by Fowkes, van Oss, and Good et al. (Wålinder 2002, Van Oss 1994, Good 1992).

The Lifschitz—van der Waals component γ_s^{LW} is obtained from Equation 8.7 for diiodomethane

$$\gamma_s^{LW} = 0.25\gamma_L^{LW}(1+\cos\theta)^2 \tag{8.7}$$

where γ_L^{LW} is the surface tension of diiodomethane from Table 8.4.

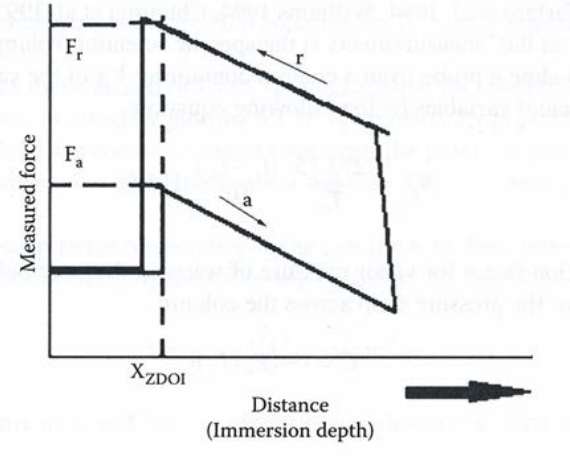

FIGURE 8.22 Schematic diagram of the immersion graph as the specimen is immersed (a) and withdrawn (r) from the liquid. The vertical broken line coincides with the point when the specimen first comes into contact with the liquid at the zero depth of immersion, $x = X_{ZDOI}$•

TABLE 8.4
Physical Data and Surface Tension Values of Selected Probe Liquids

Liquid	Density (kg/m³)	Viscosity (mPa · S)	γ_L (mJ · m⁻²)	γ_L^{LW} (mJ · m⁻²)	γ_L^+ (mJ · m⁻²)	γ_L^- (mJ · m⁻²)	γ_L^{AB} (mJ · m⁻²)
Diiodomethane	3325	2.8	50.8	50.8	0	0	0
Water	1000	1.00	72.8	21.8	25.5	25.5	51.0
Formamide	799	1.02	58.0	39.0	2.28	39.6	19.0

Source: Van Oss, C.J. 1994. *Interfacial Forces in Aqueous Media*. CRC Press, Boca Raton, FL.

Substituting the known value of γ_s^{LW} in Equation 8.8, the acid, γ_s^+, and base, γ_s^- components of the surface energy can be calculated from the advancing contact angles of water and formamide

$$0.5\gamma_L(1+\cos\theta) = (\gamma_s^{LW}\gamma_L^{LW})^{1/2} + (\gamma_s^-\gamma_L^+)^{1/2} + (\gamma_s^+\gamma_L^-)^{1/2}. \tag{8.8}$$

The total acid-base component can be calculated from Equation 8.9.

$$\gamma_s^{AB} = 2(\gamma_s^+)^{1/2}(\gamma_s^-)^{1/2}. \tag{8.9}$$

The total surface energy of the wood can be calculated from Equation 8.10.

$$\gamma_s = \gamma_s^{LW} + \gamma_s^{AB}. \tag{8.10}$$

8.4.2 INVERSE GAS CHROMATOGRAPHY (IGC)

IGC involves packing the material to be studied, typically in a fibrous or particle form, into the column of a gas chromatograph. The retention behavior of a known vapor probe, which is injected into the carrier gas that passes through the packed column, allows the solid-vapor adsorption characteristics, and thus the surface thermodynamic properties, of the material to be quantified (Schultz and Lavielle 1989, Fowkes 1990,Vg°,mdem and Reidl 1991, Lavielle and Schultz 1991, Felix and Gatenholm 1993, Kamdem et al. 1993, Farfard et al. 1994, Williams 1994, Chtourou et al. 1995, Belgacem 2000).

The key parameter in IGC measurements is the specific retention volume, $V_g°$, or the volume of carrier gas required to elute a probe from a column containing 1 g of the sample of material. $V_g°$ is related to the experimental variables by the following equation:

$$V_g° = \frac{273.15}{T_c}.\frac{(t_r - t_m)}{W}.F.J.C \tag{8.11}$$

where C is the correction factor for vapor pressure of water in the soap bubble flowmeter, and J is the correction factor for the pressure drop across the column.

$$C = 1-(P_w/P_0) \tag{8.12}$$

and

$$J = 1.5\left[\frac{(P_i/P_0)^2 - 1}{(P_i/P_0)^3 - 1}\right] \tag{8.13}$$

7', is the column temperature in K; W is the amount of material packed into the column in *g; t_r* is the retention time of the probe in min; t_m is the retention time of a reference probe such as methane or argon in min; *F* is the carrier gas flow rate in mL/min; P_w is the vapor pressure of water at the column temperature in mm Hg; P_o is the carrier gas pressure at the column outlet (atmospheric pressure) in mm Hg; P_i is the carrier gas pressure at the column inlet in mm Hg.

8.4.3 TOTAL SURFACE ENERGY

The total surface energy may be regarded as the sum of the contribution of two components, a nonpolar and a polar component. The nonpolar component is associated with London dispersive forces of interaction, and the polar component is associated with acid—base interactions.

8.4.3.1 Dispersive Component of the Total Surface Energy

The interaction of neutral probes such as saturated *n*-alkanes with the surface of the sample of the material is predominated by London dispersive forces of interaction. Under conditions of infinite dilution of the injected probe vapors, it has been shown that the dispersive component, γ_s^D of the total surface energy of the material is related to $V_g°$ by the following equation:

$$RT \ln V_g° = 2N(\gamma_s^D)^{1/2} a(\gamma_L^D)^{1/2} + C^t \tag{8.14}$$

where *Nis* Avogadro's number, *a* is the surface area of the probe molecule, γ^D_L is the dispersive component of the surface energy of the probe, Ct is a constant, which depends on the reference states.

A plot of RT In $V_g°$ versus 2N $a(\gamma^D_L)^{1/2}$ should give a straight line with slope, $(\gamma^D_s)^{1/2}$.

8.4.3.2 Acid–Base Component of the Total Surface Energy

The interaction of polar probes with the surface of the material involves both dispersive and acid-base interactions. The free energy of desorption, $\Delta G°_{AB}$, corresponding to specific acid—base interactions may be related to $V_g°$ by the following equation:

$$RT \ln(V_g° / V_g°*) = \Delta G°_{AB} \tag{8.15}$$

where $v_g°$ is the specific retention volume of the polar probe, $V_g°*$ is the specific retention volume of a reference neutral n-alkane.

This equation suggests that values of RT $1nV_g°$ plotted against 2N $a(\gamma^d_L)^{1/2}$ for polar probes should fall above the straight line obtained by plotting RT In $V_g°*$ versus 2N $a(\gamma^d_L)^{1/2}$ for the reference neutral n-alkane probes. The difference of ordinates between the point corresponding to the specific polar probe and the reference line gives the value of the free energy of desorption corresponding to the specific acid—base.

The free energy of desorption corresponding to the specific acid—base interactions may be related to the enthalpy of desorption, A1-11', by the following equation:

$$\Delta G°_{AB} = \Delta H°_{AB} — T\Delta S°_{AB} \tag{8.16}$$

where, *T* is the temperature in *K,* and $\Delta S°_{AB}$ is the entropy of desorption corresponding to the specific acid—base interactions.

A plot of $\Delta G°_{AB}/T$ versus 1/*T* should yield a straight line with slope, $\Delta H°_{AB}$.

It has been shown that the enthalpy of desorption may be used to obtain the acidic and basic constants of a substrate. The acidic and basic constants, K_A and K_B, may be regarded as the acceptor and

donor numbers, respectively, and are analogous to the acceptor number, AN*, and donor number, DN of any compound as defined by the Gutmann theory of acids and bases. The enthalpy of desorption corresponding to the specific acid-base interactions is related to K_A, K_B, AN`, and DN by the following expression:

$$\Delta H°_{AB} = K_A DN + K_B AN^*. \quad (8.17)$$

A plot of $\Delta H°_{AB}/AN^*$ versus DN/AN^* should yield a straight line with slope, K_A and intercept, K_B. Values of DN and AN* for various solvents are available in the literature.

IGC has been used to characterize the surfaces of cellulose fibers, birch wood meal, polyethylene and wood pulp fibers, synthetic polymers, and lignocellulosic fibers grafted with poly (methylmethacrylate). The values of the dispersive component of the surface energy of some lignocellulosic materials are summarized in Tables 8.5 and 8.6 summarizes values of acid—base properties, expressed in terms of the ratio, K_A/K_B. For acidic surfaces the value of this ratio is generally greater than 1.0.

TABLE 8.5
Values of the Dispersive Component of the Surfa ce Energy of Lignocellulosics Obtained under Infinite Dilution Conditions

Material	Treatment	γ^D_s at (T°C), ml/m^2	Reference
Cellulose	Untreated	48.5 (25°C)	Belgacem (2000)
Wood birch	None	43.8 (50°C)	Kamdem et al. (1993)
Bleached softwood kraft pulp	Untreated	37.9 (40°C)	Belgacem (2000)
Lignin	Kraft	46.6 (50°C)	Belgacem (2000)
Wood eastern white pine	Unextracted	37 (40°C)	Tshabalala (1997)
Kenaf powder	Unextracted	40 (40°C)	Tshabalala (1997)
Wood eastern white pine	Extracted with toluene/ethanol (2:1 v/v)	49 (40°C)	Tshabalala (1997)
Kenaf powder	Extracted with toluene/ethanol (2:1 v/v)	42 (40°C)	Tshabalala (1997)

TABLE 8.6
Acid-Base Properties of Lignocellulosic Surfaces Obtained under Infinite Dilution Conditions

Material	Treatment	K_A/K_B	Reference
Cellulose powder, 20 μm particle size	None	24	Tshabalala (1997)
Wood birch	None	1.5	Kamdem et al. (1993)
Bleached softwood kraft pulp	Untreated	2.2-5.7	Belgacem (2000)
Wood eastern white pine	Extracted with toluene/ethanol (2:1 v/v)	1.4	Tshabalala (1997)
Kenaf powder	Unextracted	0	Tshabalala (1997)
Kenaf powder	Extracted with toluene/ethanol (2:1 v/v)	1.6	Tshabalala (1997)

8.5 CONCLUSIONS AND OUTLOOK

Characterization of surface properties of wood is a very complex and difficult undertaking. No single technique is adequate to completely characterize the surface chemistry of wood and related lignocellulosic materials. Rather, a combination of spectrometric techniques used together with microscopic and thermodynamic techniques can provide good insight into the chemical composition of lignocellulosic surfaces, the surface distribution, and topography of acid-base sites, and the effect of chemical composition on the reactivity and mechanical properties of lignocellulosic surfaces. Hence, as new surface sensitive spectroscopic techniques are applied to the study of lignocellulosic surfaces, it is likely that better data will be developed that should greatly enhance our understanding of the surface chemistry of wood, and its effect on surface properties of wood, including surface mechanical properties.

REFERENCES

Adamson, A. W. 1967. *Physical Chemistry of Surfaces.* 2nded. Interscience, New York.

Adusumalli, R.-B., Mook, W., Passas, R., Schwaller, P., and Michler, J. 2010a. Nanoindentation of single pulp fibre cell walls. *Journal of Materials Science* 45(10):2558-2563.

Adusumalli, R.-B., Raghavan, R., Ghisleni, R., Zimmermann, T., and Michler, J. 2010b. Deformation and failure mechanism of secondary cell wall in Spruce late wood. *Applied Physics A: Materials Science & Processing* 100(2):447-452.

Adusumalli, R.-B., Raghavan, R., Schwaller, P., Zimmermann, T., and Michler, J. 2010c. *In situ* SEM microindentation of single wood pulp fibres in transverse direction. *Journal of Electron Microscopy* 59(5):345-349.

Agarwal, U.P. 1999. An overview of raman spectroscopy as applied to lignocellulosic materials. In: *Advances in Lignocellulosic Characterization.* Dimitris S. Argyropoulos (ed.), TAPPI Press, Atlanta, Georgia.

Agarwal, U.P. and Ralph, S.A. 1997. FT-Raman spectroscopy of wood: Identifying contributions of lignin and carbohydrate polymers in the spectrum of black spruce *(Picea mariana). Applied Spectroscopy* 51(11):1648-1655.

Ahmed, A., Adnot, A., and Kaliaguine, S. 1987. ESCA study of solid residues of supercritical extraction of *Populus tremuloides* in methanol. *Journal of Applied Polymer Science* 34:359-375.

Ahmed, A., Adnot, A., and Kaliaguin, S. 1988. ESCA analysis of partially converted lignocellulosic materials. *Journal of Applied Polymer Science* 35:1909-1919.

Asif, S.A.S., Wahl, K.J., Colton, R.J., and Warren, O.L. 2001. Quantitative imaging of nanoscale mechanical properties using hybrid nanoindentation and force modulation *Journal of Applied Physics* 90(11):5838-5838.

[illegible], M-C. and Mangin, P.J. 1995. Three-dimensional evaluation of paper surfaces using confocal microscopy. In: Surface Analysis of Paper. Terrance E. Conners and Sujit Banarjee (eds.), CRC Press, Inc. Boca Raton, Florida.

Belgacem, M.N. 2000. Characterisation of polysaccharides, lignin and other woody components by inverse gas chromatography. *Cellulose Chemistry and Technology* 34:357-383.

Benninghoven, A., Hagenhoff, B., and Niehuis, E. 1993. Surface MS: probing real-world samples. *Analytical Chemistry* 65(14):630A-640A.

Boyde, A. 1994. Bibliography on Confocal microscopy and its applications. *Scanning* 16:33-56.

Brandt, B., Zollfrank, C., Franke, 0., Fromm, J., Göken, M., and Durst, K. 2010. Micromechanics and ultrastructure of pyrolysed softwood cell walls. *Acta Biomaterialia* 6(11):4345-4351.

Brinen. J.S. 1993. The observation and distribution of organic additives on paper surfaces using surface spectroscopic techniques. *Nordic Pulp and Paper Research Journal* 8:123-129.

Brinen, J.S. and Kulick, R.J. 1995. SIMS imaging of paper surfaces. Part 4. The detection of desizing agents on hard-to-size paper surfaces. *International Journal of Mass Spectrometry Ion Processes* 143:177-190.

Cheng, Y.-T. and Cheng, C.-M. 2004. Scaling, dimensional analysis, and indentation measurements. *Materials Science & Engineering R: Reports* 44(Copyright 2005, IEE):91-149.

Chtourou, H.B., Reidel, B., and Kokta, B.V. 1995. Surface characterization of modified polyethylene pulp and wood pulp fibers using XPS and inverse gas chromatography. *Journal of Adhesion Science and Technology* 9(5):551-574.

Comyn, J. 1993. Surface analysis and adhesive bonding. *Analytical Proceedings* 30:27-28.

Conley, R.T. 1996. *Infrared Spectroscopy.* Allyn and Bacon, Boston.

Danilatos, G.D. 1988. Foundations of environmental scanning electron microscopy. *AdvAnces in Electronics and Electron Physics 71:109-250.*

Danilatos, G.D. 1993. Introduction to the ESEM Instrument. *Microscopy Research and Technique,* 25:354-361.

De Hosson, J., Soer, W., Minor, A., Shan, Z., Stach, E., Syed Asif, S., and Warren, 0. 2006. *In situ* TEM nanoindentation and dislocation-grain boundary interactions: a tribute to David Brandon. *Journal of Materials Science* 41(23):7704-7719.

De Meijer, M., Haemers, S., Cobben, W., and Militz, H. 2000. Surface energy determinations of wood: Comparison of methods and wood species. *Langmuir* 16:9352-9359.

Deshmukh, S.C. and Aydil, E.S. 1996. Investigation of low temperature $Si0_2$ plasma enhanced chemical vapor deposition. *Journal of Vacuum Science and Technology* B14:738.

Detter-Hoskin, L.D. and Busch, K.L. 1995. SIMS: Secondary ion mass spectrometry. In: *Surface Analysis of Paper.* Conners, T.E. and Banerjee, S.S. (eds), CRC Press, Inc. Boca Raton, Florida.

Donald, A.M. 2003. The use of environmental scanning electron microscopy for imaging wet and insulating materials. *Nature Materials* 2(8):511-516.

Donaldson, L. 2003. *Private Communication.* Cell Wall Biotechnology Center, Forest Research, New Zealand.

Dorris, G.M. and Gray, D.G. 1978a. The surface analysis of paper and wood fibres by ESCA I. *Cellulose Chemistry and Technology* 12:9-23.

Dorris, G.M. and Gray, D.G. 1978b. The surface analysis of paper and wood fibres by ESCA II. *Cellulose Chemistry and Technology* 12:721-734.

Farfard, M., El-Kindi, M., Schreiber, H.P., G. Dipaola-Baranyi, G., and Hor, A.M. 1994. Estimating surface energy variations of solids by inverse gas chromatography. *Journal of Adhesion Science and Technology* 8(12): 1383-1394.

Fardim P., Gustafsson J., von Schoultz S., Peltonen J., and Holmbom B. 2005. Extractives on fiber surfaces investigated by XPS, ToF-SIMS and AFM, Colloids and Surfaces A: Physicochem. *Engineering Aspects* 255:91-103.

Felix, J.M. and Gatenholm, P. 1993. Characterization of cellulose fibres using inverse gas chromatography. *Nordic Pulp and Paper Research Journal* 1:200-203.

Fischer-Cripps, A.C. 2004. *Nanoindentation.* Springer, New York.

Follrich, J., Stöckel, F., and Konnerth, J. 2010. Macro- and micromechanical characterization of wood-adhesive bonds exposed to alternating climate conditions. *Holzforschung* 64(6):705-711.

Fowkes, F.M. 1990. Quantitative characterization of the acid-base properties of solvents, polymers and inorganic surfaces. *Journal of Adhesion Science and Technology* 4(8):669-691.

Fracassi, F., d'Agostino, R., and Favia, P. 1992. Plasma-enhanced chemical vapor-deposition of organosilica thin-films from tetraethoxysilane-oxygen feeds. *Journal of the Electrochemical Society* 139(9):2936-2944.

Frisbie, C.D., Rozsnyai, L.F., Noy, A., Wrighton, M.S., and Lieber, C.M. 1994. Functional group imaging by chemical force microscopy. *Science* 265:2071-2074.

Frommer, J. 1992. Scanning tunneling microscopy and atomic force microscopy in organic chemistry. *Angewandte Chemie International Edition in English* 31:1298-1328.

Fujisawa, N. and Swain, M.V. 2008. Nanoindentation-derived elastic modulus of an amorphous polymer and its sensitivity to load-hold period and unloading strain rate. *Journal of Materials Research* 23(3):637-641.

Gacitua, W., Bahr, D., and Wolcott, M. 2010. Damage of the cell wall during extrusion and injection molding of wood plastic composites. *Composites Part A: Applied Science and Manufacturing* 41(10):1454-1460.

Gershon, A.L., Bruck, H.A., Xu, S., Sutton, M.A., and Tiwari, V. 2010. Multiscale mechanical and structural characterizations of Palmetto wood for bio-inspired hierarchically structured polymer composites. *Materials Science and Engineering: C* 30(2):235-244.

Gindl, W., Gupta, H.S., and Grunwald, C. 2002. Lignification of spruce tracheid secondary cell walls related to longitudinal hardness and modulus of elasticity using nano-indentation. *Canadian Journal of Botany* 80(10):1029-1033.

Gindl, W., Gupta, H.S., Schoberl, T., Lichtenegger, H.C., and Fratzl, P. 2004a. Mechanical properties of spruce wood cell walls by nanoindentation. *Applied Physics A (Materials Science Processing)* A79(8):2069-2073.

Gindl, W. and Schoberl, T. 2004. The significance of the elastic modulus of wood cell walls obtained from nanoindentation measurements. *Composites Part A: Applied Science and Manufacturing* 35(11):1345-1349.

Gindl, W., Schoberl, T., and Jeronimidis, G. 2004b. Erratum: The interphase in phenol-formaldehyde (PF) and polymeric methylene di-phenyl-di-isocyanate (pMDI) glue lines in wood (International Journal of Adhesion and Adhesives (2004) 24 (279-286)). *International Journal of Adhesion and Adhesives* 24(6):535-535.

Gindl, W., Schoberl, T., and Jeronimidis, G. 2004c. The interphase in phenol-formaldehyde and polymeric methylene di-phenyl-di-isocyanate glue lines in wood. *International Journal of Adhesion and Adhesives* 24(4):279-286.

Good, R.J. 1992. Contact angle, wetting, and adhesion: A critical review. *J. Adhesion Sci. Technol.* 6(12): 1269-1302.

Gray, D.G. 1978. The surface analysis of paper and wood fibres by ESCA III. *Cellulose Chemistry and Technology* 12:735-743.

Hanley, S.J. and Gray, D.G. 1994. Atomic force microscope images of black spruce wood sections and pulp fines. *Holzforschung* 48(1):29-34.

Hanley, S.J. and Gray, D.G. 1995. Atomic force microscopy. In *Surface Analysis of Paper.* Conner, T.E. and Banerjee, S.S. (eds). CRC Press, Inc. Boca Raton, Fl.

Hansma, P.K., Ellings, V.B., Marti$_3$O., and Bracker, C.E. 1998. Scanning tunneling microscopy and atomic force microscopy: *Application and Technology. Science* 242:209-216.

Herbert, E.G., Oliver, W.C., Lumsdaine, A., and Pharr, G.M. 2009. Measuring the constitutive behavior of viscoelastic solids in the time and frequency domain using flat punch nanoindentation. *Journal of Materials Research* 24(Copyright 2009, The Institution of Engineering and Technology):626-637.

Hoh, J.H. and Engel, A. 1993. Friction effects on force measurements with an atomic force microscope. *Langmuir* 9:3310-3312.

Hon, D.N.-S. 1984. ESCA study of oxidized wood surfaces. *Journal of Applied Polymer Science* 29:2777-2784.

Hon, D.N.-S and Feist, W.C. 1986. Weathering characteristics of hardwood surfaces. *Wood Science and Technology* 20:169-183.

Hua, X., Ben,Y., Kokta,B.V., and Kalinguin, S. 1991. Application of ESCA in wood and pulping chemistry. *China Pulp and Paper* 10:52-57.

Hua, X., Kaliaguine, S., Kokta, B.V., and Adnot, A. 1993a. Surface analysis of explosion pulps by ESAC. Part 1: Carbon (1s) spectra and oxygen-to-carbon ratios. *Wood Science and Technology* 27:449-459.

Hua, X., Kaliaguine, S., Kokta, B.V., and Adnot, A. 1993b. Surface analysis of explosion pulps by ESAC. Part 2: Oxygen (1s) and sulfur (2p) spectras. *Wood Science and Technology* 28:1-8.

Jager, A., Bader, T., Hofstetter, K., and Eberhardsteiner, J. 2011. The relation between indentation modulus, microfibril angle, and elastic properties of wood cell walls. *Composites Part A: Applied Science and Manufacturing* 42(6):677-685.

Jakes, J.E., Frihart, C.R., Beecher, J.F., Moon, R.J., Resto, P.J., Melgarejo, Z.H., Surez, 0.M., Baumgart, H., Elmustafa, A.A., and Stone, D.S. 2009a. Nanoindentation near the edge. *Journal of Materials Research* 24(3):1016-1031.

Jakes, J.E., Frihart, C.R., Beecher, J.F., Moon, R.J., and Stone, D.S. 2008a. Experimental method to account for structural compliance in nanoindentation measurements. *Journal of Materials Research* 23(4):1113-1127.

Jakes, J.E., Frihart, C.R., and Stone, D.S., 2008b. Creep properties of micron-size domains in ethylene glycol modified wood across 4 1/2 decades in strain rate. In: Katti, K., Hellmich, C., Wegst, U.G.K., Narayan, R. (eds.). *Materials Research Society. Mater. Res. Soc. Symp. Proc.,* Boston, MA, USA, p. 1132Z0721.

Jakes, J.E., Lakes, R., and Stone, D.S. 2011a. Broadband Nanoindentation I: Viscoelasticity of glassy polymers. *Journal of Materials Research* 27(2):463-474.

Jakes, J.E., Lakes, R., and Stone, D.S. 2011b. Broadband nanoindentation II: Viscoplasticity of glassy polymers *Journal of Materials Research* 27(2):475-484.

Jakes, J.E. and Stone, D.S. 2011. The edge effect in nanoindentation. *Philosophical Magazine* 91(7): 1387-1399.

Jakes, J.E., Yelle, D.J., Beecher, J.F., Frihart, C.R., and Stone, D.S., 2009b. Characterizing pMDI reactions with wood cell walls: 2. Nanoindentation. In: Frihart, C.R., Hunt, C.G., Moon, R.J. (eds.). *International Conference on Wood Adhesives.* Forest Products Society, Harveys Resort & Casino, Lake Tahoe, Nevada, USA *(submitted),* pp. 366-373.

Johnson, K.L. 1985. *Contact Mechanics*. Cambridge University Press, Cambridge, UK.

Johnson, D. and Hibbert, S. 1992. Applications of secondary ion mass spectrometry (SIMS) for the analysis of electronic materials. *Semiconductor Science and Technology* 7:A180-A184.

Kamdem, D.P., Bose, S.K., and Luner, P. 1993. Inverse gas chromatography of birch wood meal. *Langmuir* 9:3039-3044.

Kamdem, D.P. and Reidl, B. 1991. IGC characterization of PMMA grafted onto CTMP fiber. *Journal of Wood Chemistry and Technology 11(1):57-91.*

Kamdem, D.P., Reidl, B., Adnot, A., and Kaliaguine, S. 1991. ESCA spectroscopy of poly(methyl methacrylate) grafted onto wood fibers. *Journal of Applied Polymer Science* 43:1901-1912.

Kangas H. 2007. Surface chemical and morphological properties of mechanical pulps, fibers and fines, November, KCL Communications 13.

Konnerth, J., Buksnowitz, C., Gindl, W., Hofstetter, K., and Jager, A., 2010a. Full Set of Elastic Constants of Spruce Wood Cell Walls Determined by Nanoindentation. International Convention of Wood Science and Technology and United Nations Economic Commission for Europe-Timber Committee, Geneva, Switzerland.

Konnerth, J., Eiser, M., Jäger, A., Bader, T.K., Hofstetter, K., Follrich, J., Ters, T., Hansmann, C., and Wimmer, R. 2010b. Macro- and micro-mechanical properties of red oak wood (Quercus rubra L.) treated with hemicellulases. *Holzforschung* 64(4):447-453.

Konnerth, J. and Gindl, W. 2006. Mechanical characterisation of wood-adhesive interphase cell walls by nanoindentation. *Holzforschung* 60(4):429-433.

Konnerth, J. and Gindl, W. 2008. Observation of the influence of temperature on the mechanical properties of wood adhesives by nanoindentation. *Holzforschung* 62(6):714-717.

Konnerth, J., Harper, D., Lee, S.-H., Rials, T.G., and Gindl, W. 2008. Adhesive penetration of wood cell walls investigated by scanning thermal microscopy (SThM). *Holzforschung* 62(1):91-98.

Konnerth, J., Jager, A., Eberhardsteiner, J., Muller, U., and Gindl, W. 2006. Elastic properties of adhesive polymers. II. Polymer films and bond lines by means of nanoindentation. *Journal of Applied Polymer Science* 102:1234-1239.

Konnerth, J., Valla, A., and Gindl, W. 2007. Nanoindentation mapping of a wood-adhesive bond. *Applied Physics A: Materials Science and Processing* 88(2):371-375.

Lahiji, R.R., Xu, X., Reifenberger, R., Raman, A., Rudie, A., and Moon, R.J. 2010. Atomic force microscopy characterization of cellulose nanocrystals. *Langmuir* 26(6):4480-4488.

Lavielle, L. and Schultz, J. 1991. Surface properties of carbon fibers determined by inverse gas chromatography. *Langmuir* 7(5):978-981.

Lee, B.H., Kim, H., Lee, J.J., and Park, M.J. 2003. Effects of acid rain on coatings for exterior wooden panels. *Journal of Industrial and Engineering Chemistry,* 9(5):500-507.

Lehringer, C., Koch, G., Adusumalli, R.-B., Mook, W.M., Richter, K., and Militz, H. 2011. Effect of physisporinus vitreus on wood properties of Norway spruce. Part 1: Aspects of delignification and surface hardness. *Holzforschung,* 65(5):711-719.

Leica TCS Confocal Systems User Manual, 1999. Version 1.0, January, Leica Microsystems Heidelberg GmbH. Edited and written by EDV-Service Dr. Kehrel, Heidelberg, Germany.

Li, J-X. and Gardella, J.A. Jr. 1994. Quantitative static secondary ion mass spectrometry of pH effects on octadecylamine monolayer Langmuir-Blodgett films. *Analytical Chemistry* 66(7):1032-1037.

Libermann, M.A. and Lichtenberg, A.J. 1994. *Principles of Plasma Discharges and Materials Processing.* Wiley, New York.

Lichtman, J.W. 1994. Confocal microscopy. *Scientific American* 271:40-45.

Loubet, J.L., Oliver, W.C., and Lucas, B.N. 2000. Measurement of the loss tangent of low-density polyethylene with a nanoindentation technique. *Journal of Materials Research* 15(5):1195-1198.

Louder, D.R. and Parkinson, B.A. 1995. An update on scanning force microscopies. *Analytical Chemistry* 67 (9): 297A-303A.

Loxton, C., Thumm, A., Grisby, W.J., Adams, T.A., and Ede, R.M. 2003. Resin distribution in medium density fiberboard. Quantification of OF resin distribution on blowline- and dry-blended MDF fiber and panels. *Wood and Fiber Science* 35(3):370-380.

McGhie, A.J., Tang, S.L., and Li, S.F.Y. 1995. Expanding the uses of AFM. *Chemtech* 25(7):20-26.

Meredith, P., Donald, A.M., and Thiel, B. 1996. Electron-gas interactions in the environmental SEM's gaseous detector. *Scanning* 18:467-473.

Meyer, E. 1992. Atomic force microscopy. *Progress in Surface Science* 41:3-49.

Minor, A.M., Morris, J.W., and Stach, E.A. 2001. Quantitative *in situ* nanoindentation in an electron microscope. *Applied Physics Letters* 79(11):1625-1627.

Mirabella, F.M. (ed.) 1998. *Modern Techniques in Applied Molecular Spectroscopy.* John Wiley Publications, New York.

Mjörberg, P.J. 1981. Chemical surface analysis of wood fibres by means of ESCA. *Cellulose Chemistry and Technology* 15:481-486.

Nguyen, T. and Johns, W.E. 1978. Polar and dispersion force contributions to the total surface free energy of wood. *Wood Science and Technology* 12:63-74.

Oliver, W.C. and Pharr, G.M. 1992. Improved technique for determining hardness and elastic modulus using load and displacement sensing indentation experiments. *Journal of Materials Research* 7(6):1564-1580.

Oliver, W.C. and Pharr, G.M. 2004. Measurement of hardness and elastic modulus by instrumented indentation: Advances in understanding and refinements to methodology. *Journal of Materials Research* 19(1):3-20.

Oyen, M.L. 2011. Mechanics of indentation. In: Oyen, M.L. (ed.), *Handbook of Nanoindentation with Biological Applications*. Pan Stanford, Singapore, pp. 123-152.

Pachuta, S.J. and Staral, J.S. 1994. Nondestructive analysis of colorants on paper by time-of-flight secondary ion mass spectrometry. *Analytical Chemistry* 66(2):276-284.

Pandey, K.K. and Theagarajan, K.S. 1997. Analysis of wood surfaces and ground wood by diffuse reflectance (DRIFT) and photoacoustic (PAS) Fourier transform spectroscopic techniques. *Holz als Roh- and Werkstoff* 55:383-390.

Pawley, J.B. 1990. *The Handbook of Biological Confocal Microscopy.* Plenum, New York.

Perry, S.S. and Somorjai, G.A. 1994. Characterization of organic surfaces. *Analytical Chemistry* 66(7):403A-415A.

Puthoff, J.B., Jakes, J.E., Cao, H., and Stone, D.S. 2009. Investigation of thermally activated deformation in amorphous PMMA and Zr-Cu-Al bulk metallic glasses with broadband nanoindentation creep. *Journal of Materials Research* 24(3):1279-1290.

Rynders. R.M., Hegedus, C.R., and Gilicinski, A.G. 1995. Characterization of particle coalescence in water-borne coatings using atomic force microscopy. *Journal of Coatings Technology* 667(845):59-69.

Sahli, S., Segui,Y., Ramdani,R., and Takkouk, Z. 1994. RF plasma deposition from hexamethyldisiloxane oxygen mixtures. *Thin Solid Films* 250(1-2):206-212.

Schaefer, D.M., Carpenter, M., Gady, B., Reifenberger, R., Demejo, L.P., and Rimai, D.S. 1995. Surface roughness and its influence on particle adhesion using atomic force techniques. *Journal of Adhesion Science and Technology* 9(8):1049-1062.

Selamoglu, N., Mucha, J.A., Ibbotson, D.E., and Flamm, D.L. 1989. Silicon oxide deposition from tetraethoxysilane in radio frequency: Downstream reactor: Mechanism and step coverage. *Journal of Vacuum Science and Technology* B7:1345.

Schultz, J. and Lavielle, L. 1989. Interfacial properties of carbon fiber-epoxy matrix composites. In: *Inverse Gas Chromatography, ACS Symposium Series.* Lloyd, D.R., Ward, T.C., and Schreiber, H.P. (eds). American Chemical Society, Washington, D.C. 391:168-184.

Stanzl-Tschegg, S., Beikircher, W., and Loidl, D. 2009. Comparison of mechanical properties of thermally modified wood at growth ring and cell wall level by means of instrumented indentation tests. *Holzforschung* 63(4):443-448.

Stöckel, F., Konnerth, J., Kantner, W., Moser, J., and Gindl, W. 2010a. Mechanical characterisation of adhesives in particle boards by means of nanoindentation. *European Journal of Wood and Wood Products* 68(4):421-426.

Stöckel, F., Konnerth, J., Kantner, W., Moser, J., and Gindl, W. 2010b. Tensile shear strength of UF- and MUF-bonded veneer related to data of adhesives and cell walls measured by nanoindentation. *Holzforschung* 64(3):337-342.

Stone, D.S., Yoder, K.B., and Sproul, W.D. 1991. Hardness and elastic modulus of TiN based on continuous indentation technique and new correlation. *Journal of Vacuum Science & Technology A (Vacuum, Surfaces, and Films)* 9(4):2543-2547.

Stuart, B.H. 2004. *Infrared Spectroscopy-Fundamentals and Applications*. John Wiley Publications, New York.

Sundqvist B., Doctoral thesis 2004. *Colour Changes and Acid Formation in Wood During Heating.* Lulea University of Technology, Sweden.

Tan, Z. and Reeve, D.W. 1992. Spatial distribution of organochlorine in fully bleached haft pulp fibres. *Nordic Pulp and Paper Research Journal* 6:30-36.

Tang, B. and Ngan, A.H.W. 2003. Accurate measurement of tip-sample contact size during nanoindentation of viscoelastic materials. *Journal of Materials Research* 18(Copyright 2003, IEE):1141-1148.

Tokareva E. 2011. *Doctoral thesis - "Spatial Distribution of Components in Wood by ToF-SIMS".* Abo Akademi University, Turku.

Tshabalala, M.A. 1997. Determination of acid-base characteristics of lignocellulosic surfaces by inverse gas chromatography. *Journal of Applied Polymer Science* 65:1013-1020.

Tshabalala, M.A., Kingshott, P., VanLandingham, M.R., and Plackett, D. 2003. Surface chemistry and moisture sorption properties of wood coated with multifunctional alkoxysilanes by sol-gel process. *Journal of Applied Polymer Science* 88(12):2828-2841.

Tze, W.T.Y., Wang, S., Rials, T.G., Pharr, G.M., and Kelley, S.S. 2007. Nanoindentation of wood cell walls: Continuous stiffness and hardness measurements. *Composites Par t A: Applied Science and Manufacturing* 38(3):945-953

VanLandingham, M.R., Chang, N.K., Drzal, P.L., White, C.C., and Chang, S.H. 2005. Viscoelastic characterization of polymers using instrumented indentation. I. Quasi-static testing. *Journal of Polymer Science, Part B (Polymer Physics)* 43(Copyright 2006, IEE):1794-1811.

Van Oss, C.J. 1994. *Interfacial Forces in Aqueous Media.* CRC Press, Boca Raton, FL.

Viitaneimi P., Thmsa S., Ek P., and Viitanen H. 2001. Method for increasing the resistance of cellulosic products against mould and decay, EP695408B1.

Vlassak, J.J., Ciavarella, M., Barber, J.R., and Wang, X. 2003. The indentation modulus of elastically anisotropic materials for indenters of arbitrary shape. *Journal of the Mechanics and Physics of Solids* 51(9):1701-1721.

Wålinder. M.E.P. 2002 Study of lewis acid-base properties of wood by contact angle analysis. *Holzforschung,* 56:363-371.

Watts, J.F. 1990. *An Introduction to Surface Analysis by Electron Spectroscopy.* Oxford University Press, New York.

Watts, J.F. 1992. Investigation of adhesion phenomena using surface analytical techniques. *Analytical Proceedings* 29:396-398.

Williams, D. 1994. Inverse gas chromatography. In: *Characterization of Composite Materials.* H. Ishida (ed.), Butterworth-Henemann, Boston, MA.

Williams, R.S. and Feist, W.C. 1984. Application of ESCA to evaluate wood and cellulose surfaces modified by aqueous chromium trioxide treatment. *Colloids and Surfaces* 9:253-271.

Wimmer, R. and Lucas, B.N. 1997. Comparing mechanical properties of secondary wall and cell corner middle lamella in spruce wood. *Iawa Journal* 18(1):77-88.

Wimmer, R., Lucas, B.N., Tsui, T.Y., and Oliver, W.C. 1997. Longitudinal hardness and Young's modulus of spruce tracheid secondary walls using nanoindentation technique. *Wood Science and Technology* 31(2):131.

Winograd, N. 1993. Ion beams and laser positionization for molecule-specific imaging *Analytical Chemistry* 65(14):622A-629A.

Wang, S. and Peltonen, J. 2011. Surface characterization of wood samples by ToF-SIMS. *Private Communication.*

Wu, Y., Wang, S., Zhou, D., Xing, C., and Zhang, Y. 2009. Use of nanoindentation and silviscan to determine the mechanical properties of 10 hardwood species. *Wood and Fiber Science* 41(1):64-73.

Xing, C., Wang, S., and Pharr, G. 2009. Nanoindentation of juvenile and mature loblolly pine wood fibers as affected by thermomechanical refining pressure. *Wood Science and Technology* 43(7):615-625.

Young, R.A., Rammon, R.M., Kelley, S.S., and Gillespie, R.H. 1982. Bond formation by wood surface reactions. Part I: Surface analysis by ESCA. *Wood Science* 14:100-119.

Yu, Y., Fei, B., Wang, H., and Tian, G. 2010. Longitudinal mechanical properties of cell wall of Masson pine (Pinus massoniana Lamb) as related to moisture content: A nanoindentation study. *Holzforschung* 65(1):121-126.

Zickler, G.A., Schoberl, T., and Paris, 0. 2006. Mechanical properties of pyrolysed wood: A nanoindentation study. *Philosophical Magazine* 86(10):1373-1386.

Handbook of Wood Chemistry and Wood Composites

SECOND EDITION

Edited by Roger M. Rowell

CRC Press
Taylor & Francis Group
Boca Raton London New York

CRC Press is an imprint of the
Taylor & Francis Group, an informa business

CRC Press
Taylor & Francis Group
6000 Broken Sound Parkway NW, Suite 300
Boca Raton, FL 33487-2742

Printed in the United States of America on acid-free paper
Version Date: 20120725

International Standard Book Number: 978-1-4398-5380-1 (Hardback)

Visit the Taylor & Francis Web site at
http://www.taylorandfrancis.com

and the CRC Press Web site at
http://www.crcpress.com